

Nonlinear Modeling of Forced Magnetic Reconnection in Slab Geometry with NIMROD

M. T. Beidler, J. D. Callen, C. C. Hegna, and C. R. Sovinec

*Department of Engineering Physics, University of Wisconsin, Madison, WI 53706, USA**

The nonlinear, extended-magnetohydrodynamic (MHD) code NIMROD is benchmarked with the theory of time-dependent forced magnetic reconnection (FMR) induced by small resonant fields in slab geometry in the context of visco-resistive MHD modeling. Linear computations agree with time-asymptotic, linear theory of flow screening of externally-applied fields. The inclusion of flow in nonlinear computations can result in mode penetration due to the balance between electromagnetic and viscous forces in the time-asymptotic state, which produces bifurcations from a high-slip state to a low-slip state as the external field is slowly increased. We reproduce mode penetration and unlocking transitions by employing time-dependent externally-applied magnetic fields. Mode penetration and unlocking exhibit hysteresis and occur at different magnitudes of applied field. We also establish how nonlinearly-determined flow screening of the resonant field is affected by the square of the magnitude of the externally-applied field. These results emphasize that the inclusion of nonlinear physics is essential for accurate prediction of the reconnected field in a flowing plasma.

I. INTRODUCTION

The successful operation of ITER is threatened by deleterious transient events known as edge localized modes (ELMs) [1, 2]. It has been observed that the use of externally-imposed resonant magnetic perturbations (RMPs) may help to mitigate and even avoid these deleterious events (*e.g.*, [3–6]). A central issue in understanding RMPs is to understand forced magnetic reconnection (FMR) processes on resonant surfaces in the tokamak pedestal region.

The FMR in a tokamak is sensitive to flows local to the driven resonant surface that generally decreases the amount of reconnected RMP field. In other words, local flows screen out the external field at the resonant surface. Nonlinearly, flow at the resonant surface evolves self-consistently in accordance with electromagnetic forces and shielding currents. Under the proper conditions, this nonlinear flow evolution plays an integral role in mode penetration and locking. This context motivates the need to employ nonlinear computations to study the physics of FMR, flow screening, and mode penetration and locking in tokamaks.

To date, the majority of simulation work on the effects of RMPs on tokamak pedestals has focused on linear computations, which leave out nonlinear physics. The present work builds on previous results of FMR in slab geometry by employing nonlinear computations using the extended-MHD code NIMROD. Benchmarking NIMROD in slab geometry with well developed analytical models is a necessary first step before moving to toroidal geometry calculations where there is less analytical development.

The theory of FMR is first developed by Hahm and Kulsrud [7, 8], treating Taylor’s problem of a linearly-sheared magnetic field in a stable slab geometry configuration with tearing stability parameter $\Delta' < 0$ [9]. By perturbing the edge boundaries with a small displacement, reconnection is forced at the surface where the

perturbation is resonant.

This problem is analytically tractable, with the constant equilibrium current density profile reducing the time-independent problem to solving Laplace’s equation for the magnetic flux function ψ satisfying $\mathbf{B} = \hat{z} \times \nabla\psi$. Furthermore, analytic expressions for the evolution are obtained in separate ideal and resistive regimes where the linear approximation holds (phases A, B, and C in Ref. [8]), and for the nonlinear regime where Rutherford evolution [10] occurs. Wang and Bhattacharjee [11] include the nonlinear physics introduced in Ref. [12] to properly explain the dynamics of strongly driven FMR. Additional studies of the conversion of magnetic energy to thermal energy in FMR [13] treat marginally stable magnetic configurations with $\Delta' \lesssim 0$ and also configurations with non-uniform magnetic shear.

Much of the phenomena associated with FMR at resonant surfaces in a rotating tokamak plasma caused by externally-applied resonant magnetic fields can be understood by using the MHD cylindrical model of Refs. [14, 15]. These models are derived for a plasma under the influence of external field errors (FEs), but are equally valid for all externally-applied fields. In this model, the magnetic fields in the plasma in the time-asymptotic steady state are described by the linear superposition of the tearing (visco-resistive-MHD) and fully screened (ideal-MHD) responses. The fully screened ideal MHD response matches the externally applied field at the boundary and is zero at the resonant surface. Visco-resistive MHD effects allow the resonant field to produce FMR (tearing of the magnetic field) locally at the resonant surface. Asymptotic matching of the total field response in the bulk plasma to the tearing response in the vicinity of the resonant surface leads to a relation between the normal field at the resonant surface due to FMR and the externally applied field.

Including resistivity, viscosity and plasma flows, Ref. [15] predicts that the balance of electromagnetic and viscous torques in steady-state can lead to a torque-balance bifurcation. In this model, an initial high-slip (large flow relative to externally-applied field) state can transition to a low-slip state for a relatively small change in the externally applied field. This bifurcation exhibits

* Emails to: beidler@wisc.edu

hysteresis and a strong dependence on the relative magnitudes of applied 3D field, resistivity, viscosity, and flow [16]. More recent studies have explored the effects of flow on FMR by incorporating additional physics into the single-fluid visco-resistive model [17–26].

Experimental work in the DIII-D tokamak pioneered the effects of RMPs by applying various external fields [3–6]. In particular, recent experimental results show evidence of a high confinement (H-mode) pedestal bifurcation as the externally applied resonant component of an $n = 2$ RMP is slowly increased and causes a FMR response at the $q = m/n = 8/2 = 4$ resonant surface [27, 28]. Reference [28] also shows that the ELM suppressed state exhibits locked-mode-like magnetic signals. The appearance of a strong $n = 1$ signal in addition to the expected $n = 2$ signal perhaps indicates that nonlinear physics is playing a role, or else an $n = 1$ error field may be significant.

Building on the theoretical work of FMR in cylindrical systems, a recent study [29] develops a comprehensive, dynamical model of FMR in toroidal geometry; it finds good agreement with the aforementioned experimental results of suppression of ELMs by RMPs [27, 28]. Additional experimental observations of DIII-D low confinement (L-mode) discharges exhibit multiple $n = 1$ island bifurcations at low torque when using $n = 1$ FE correction RMP coils [30]. In this study, parametric scans over rotation show that low rotation discharges are more susceptible to tearing modes and bifurcation into a low-slip, locked mode state. A similar qualitative trend exhibiting significant reconnected field at low rotation has also been recently reported for ITER baseline scenario discharges in H-mode [31].

A significant number of numerical studies of FMR explore the magnetic field response to RMP application in 3D toroidal geometries. Studies investigate the linear [32–42] and nonlinear [43–53] field response to RMPs. Each work details studies on the physics of reconnection and flow-screening in tokamaks, and a number of the nonlinear studies discuss the interaction of RMPs with ELMs. Interestingly though, aside from one validation study [54], to our knowledge there has been minimal numerical investigation into the physics of nonlinear mode penetration due to RMPs.

Slab geometry FMR has also been studied using computational methods. Some of the earliest work utilizes 2D, reduced-MHD, tokamak simulations with simulated external coils to stimulate FMR [55]. In another study, reconnection is continuously driven in computations by injecting plasma and magnetic flux through the boundary [56]. This study includes the first observation of plasmoids with exceptionally strong driving. The Taylor problem is numerically investigated in multiple studies: Ref. [57] essentially models the FMR process, but focuses on the interaction of flows with magnetic islands; Ref. [58] explores various nonlinear effects in FMR; Ref. [59] models FMR using a large applied field in a large magnetic Prandtl number ($P_m \gg 1$) regime verifying aspects of Ref. [8] and Ref. [11]; Ref. [60] verifies the resistive-inertial (low viscosity) evolution of Ref. [8]; and Ref. [61] extends the theory of the Taylor problem to the plasmoid-

unstable regime. Computational studies of FMR are also performed in the space plasma community, including simulations of FMR in the magnetotail [62], energy release due to FMR in the solar corona [63], and a multiple code benchmark known as the Newton challenge [64].

In this paper, we extend the previous computational efforts of the aforementioned slab geometry studies by first verifying the extended-MHD code NIMROD [65] with analytic predictions of FMR and then presenting novel results from nonlinear calculations. The remainder of the paper is organized as follows: section II provides a description of the NIMROD code and computation initialization. Code verification with key aspects of FMR evolution from Ref. [8] is presented in section III. Section IV discusses additional code verification results for linear flow screening and comparisons to analytical predictions of Ref. [16]. Nonlinear mode penetration is discussed in section V by examining several topics including the consistency of time-asymptotic states with nonlinear force balance [15], direct confirmation of the hysteresis associated with a bifurcation enabled by employing time-dependent RMPs, and a contrast of flow scaling and the amount of reconnection between linear and nonlinear computations. A section containing conclusions and discussion closes the paper.

II. NUMERICAL COMPUTATION SETUP

A. The NIMROD Code

The NIMROD code [65] solves the extended-MHD equations. Here, we use NIMROD to solve the visco-resistive MHD equations given by:

$$\rho \left(\frac{\partial \mathbf{V}}{\partial t} + \mathbf{V} \cdot \nabla \mathbf{V} \right) = \mathbf{J} \times \mathbf{B} - \nabla \cdot \mathbf{\Pi}_i, \quad (1a)$$

$$\frac{\partial \mathbf{B}}{\partial t} = -\nabla \times \mathbf{E} + \kappa_{divbd} \nabla \nabla \cdot \mathbf{B}, \quad (1b)$$

$$\mathbf{E} = -\mathbf{V} \times \mathbf{B} + \eta \mathbf{J}, \quad (1c)$$

$$\mu_0 \mathbf{J} = \nabla \times \mathbf{B}. \quad (1d)$$

The single-fluid velocity \mathbf{V} , and magnetic field \mathbf{B} are evolved in time using a time-centered, semi-implicit leapfrog algorithm, which allows use of time steps exceeding the CFL condition. Equation (1a) describes the evolution of the single-fluid velocity with mass density $\rho = nM_i$, where the particle density n is held constant in time. Equation (1b) is Faraday’s law for the evolution of the magnetic field. Equation (1c) is the resistive-MHD Ohm’s law, where η is the electrical resistivity and \mathbf{J} is the current density. Lastly, Eq. (1d) is Ampère’s law for current density. The quantity κ_{divbd} is introduced to control numerical divergence error [65]. The dissipation parameter ν in $\mathbf{\Pi}_i \equiv -\rho\nu[\nabla \mathbf{V} + \nabla \mathbf{V}^T - (2/3)\nabla \cdot \mathbf{V}]$ within Eq. (1a) describes the isotropic viscosity, in which $\nabla \mathbf{V}^T$ is the transpose of $\nabla \mathbf{V}$. We note that we are simulating a cold plasma in this study, by setting $\beta \equiv p/(B^2/2\mu_0) = 0$.

Computations use the semi-implicit methods described in [65, 66], where the equilibrium fields are held constant and perturbation fields are evolved. NIMROD is a 3D

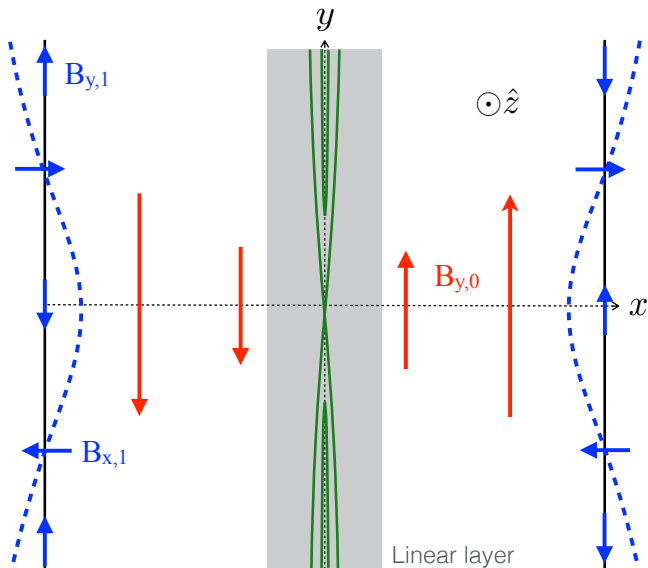


FIG. 1. Schematic of Taylor’s problem [8] for FMR in a slab geometry. Sheared magnetic fields shown in red are initially in a stable configuration with $\Delta' < 0$, which is driven by an edge perturbation magnetic field shown in blue. This forces magnetic reconnection and the generation of a magnetic island, shown in green, that is within or exceeds the linear layer, represented by the gray region, depending on the magnitude of the edge perturbation.

code that is used to solve the system of equations (1a-d) in 2D. For the majority of the calculations, perturbation fields are numerically represented in two dimensions by employing one-dimensional spectral elements of arbitrary polynomial degree along with a truncated Fourier series representation in the second dimension. This expansion is explicitly defined as

$$\mathbf{A}(x, y, t) \equiv \mathbf{A}_0(x, t) + \sum_{n=1}^N \left[\mathbf{A}_n(x, t) e^{i \frac{2\pi n}{L_y} y} + \mathbf{A}_n^*(x, t) e^{-i \frac{2\pi n}{L_y} y} \right], \quad (2)$$

where the superscript $*$ indicates a complex-conjugate. The expansion coefficients \mathbf{A}_n of perturbation fields are complex, and the wavenumber of a chosen Fourier mode is given by $k_y(n) = 2\pi n/L_y$, where the mode number is not to be confused with the particle density. The x dimension is composed of 1D spectral elements for the geometry in Fig. 1. Linear computations keep a single Fourier mode and nonlinear computations use a finite Fourier series consisting of N modes. In these computations, we use a single Fourier component to apply the magnetic perturbation, in a way similar to the analytics of Ref. [8]. However, for convenience, computations reported in sections VB and VC use 2D spectral elements in the (x, y) plane. In this representation, the perturbation is applied with 2D spectral elements, rather than with a Fourier mode.

All physical quantities appearing hereafter are written in dimensionless form. Their normalizations are derived from a characteristic length, density, and magnetic field of $L_{\text{norm}} = 1$ m, $n_{\text{norm}} = 10^{19}$ particles m^{-3} , and $B_{\text{norm}} =$

0.1 T. This sets the normalization for velocity to $V_{\text{norm}} = B_{\text{norm}}/(\mu_0 n_{\text{norm}} M_i)^{1/2} = 6.89 \times 10^5$ m/s, which is the Alfvén speed based on the characteristic magnetic field and density for hydrogen, and the time to $t_{\text{norm}} \equiv \tau_A = L_{\text{norm}}/V_{\text{norm}} = 1.45 \mu\text{s}$, the characteristic Alfvén time. The normalization used for the dissipation parameters κ_{divbd} , ν , and η/μ_0 is $D_{\text{norm}} = L_{\text{norm}}^2/t_{\text{norm}} = 6.89 \times 10^5$ m^2/s .

B. Initialization and Optimization

A schematic of the computation initialization is shown in Fig. 1. All computations are run with a domain having dimensions $(L_x, L_y) = (2, 2) L_{\text{norm}}$, so that $k_y(n) = n\pi L_{\text{norm}}^{-1}$. Adopting terminology consistent with the magnetic reconnection geometry, we refer to the x direction as the “inflow” direction, whose half width is parameterized by $a \equiv L_x/2 = L_{\text{norm}}$, and the y direction as the “outflow” direction (as in *e.g.*, [67, 68]). We use a representation with 96 quartic spectral elements in the inflow direction at $|x| = 0$ and a , where the minimum grid spacing is approximately $7.5 \times 10^{-3} L_{\text{norm}}$. We have run additional computations to verify that this mesh packing is sufficient to resolve the dominant physical mechanisms under examination in this study.

We initialize the computations in accord with Taylor’s problem, shown in Fig. 1. The (red) equilibrium magnetic field is directed in the y direction and has a linearly-sheared profile in the x direction, with an out-of-plane field in the z direction, referred to as the “guide-field.” Note that equilibrium quantities are denoted by subscript 0. The magnetic field profile for this force-free equilibrium $\mu_0 \mathbf{J}_0 = \lambda \mathbf{B}_0$ is generated by setting the guide field at $x = 0$ to $B_{z,0} = 100 B_{\text{norm}}$, the field normal to the rational surface throughout to the computational domain to $B_{x,0} = 0$, and numerically integrating the chosen parallel current profile

$$\lambda \equiv \frac{\mu_0 \mathbf{J}_0 \cdot \mathbf{B}_0}{B_0^2} = \frac{\lambda_0}{a} \text{sech}^2 \left(\frac{\lambda_0 x}{a \sin(\phi_b)} \right), \quad (3)$$

with $\lambda_0 = 0.01$ and $\phi_b = 0.5$; this yields a nearly linear profile of $B_{y,0}(x)$ with $B_{y,0}(x = \pm a) = \pm 1 B_{\text{norm}}$. From Ref. [9], a linearly sheared magnetic profile with $k_{y,n=1} a = \pi$ has a tearing stability index $a\Delta' \simeq -2\pi$, whose negative value implies stability. Higher mode numbers n are more stable. The Alfvén time τ_A , which we cite, is based on a and B_{norm} , the sheared magnetic field strength at the boundary.

This equilibrium is perturbed by a spatially non-uniform (blue) edge magnetic field, which has components normal (\hat{x}) and tangential (\hat{y}) to the resonant surface at $x = 0$. The value of the “applied field” normal to the $|x| = a$ boundary is held fixed and is parameterized by B_{ext} , while the rest of the system evolves in time. Initial profiles for the perturbation are consistent with the solution of a vacuum boundary-value problem in an edge region of width Δ , which is chosen as the outer two elements for the computations in this study. In vacuum, Ampère’s law simplifies to $\nabla \times \mathbf{B} = \mathbf{0}$, which is

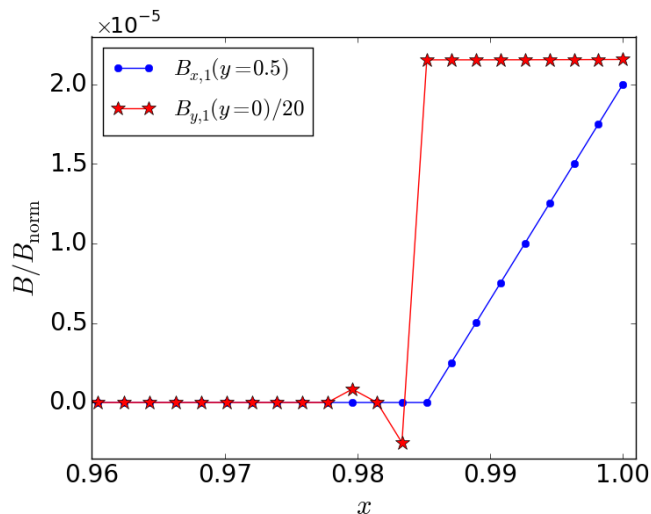


FIG. 2. Spatially non-uniform, applied fields are found by solving Laplace’s equation in an edge region along the boundary of the computation domain. The blue data indicate the normal applied field, for a value $B_{\text{ext}} = 2 \times 10^{-5} B_{\text{norm}}$ at the boundary, while the red data indicate the tangential field needed to ensure this magnetic perturbation is divergenceless.

satisfied by a magnetic field written in terms of a scalar flux function as $\mathbf{B} = -\nabla\varphi$. Solving Laplace’s equation $\nabla^2\varphi = 0$ in the edge region from $|x| = a - \Delta$ to $|x| = a$ with suitable boundary conditions yields the form of our perturbation. For the slab geometry, the solution is a linear combination of sinh and cosh functions. Choosing boundary conditions

$$B_{x,1}(|x| = a - \Delta) = 0, \quad (4a)$$

$$B_{x,1}(|x| = a) = \frac{B_{\text{ext}}}{2} (-ie^{ik_y y} + ie^{-ik_y y}), \quad (4b)$$

on the inner and outer boundary of the edge region gives perturbation profiles consistent with the phasing in Fig. 1. In the edge regions it yields

$$B_{x,1}(x, y) = \pm B_{\text{ext}} \frac{\sinh[k_y(x - a + \Delta)]}{\sinh(k_y \Delta)} \sin(k_y y), \quad (5a)$$

$$B_{y,1}(x, y) = \pm B_{\text{ext}} \frac{\cosh[k_y(x - a + \Delta)]}{\sinh(k_y \Delta)} \cos(k_y y), \quad (5b)$$

where $B_{-n} = B_n^*$, which makes the fields real. Here $+$ corresponds to perturbations in the region $a - \Delta < x < a$, and $-$ corresponds to perturbations in the region $-a < x < -a + \Delta$; thus the normal perturbation field has even parity $B_{x,1}(x) = B_{x,1}(-x)$ and the tangential perturbation field has odd parity $B_{y,1}(x) = -B_{y,1}(-x)$. Their implementation in NIMROD is exhibited in Fig. 2, where the normal field is in blue and the tangential field in red. This magnetic boundary perturbation is related to the boundary displacement perturbation of Ref. [8] by

$$\delta_{\text{HK}} = \frac{B_{\text{ext}}}{B_{y,0}(x=a) k_y} \Rightarrow \frac{B_{\text{ext}}}{\pi B_{y,0}(x=a)}. \quad (6)$$

The tangential component of the field can be seen to have some numerical overshoot in the element adjacent

to the edge region because NIMROD is not designed for treating discontinuities. This initialization drives additional modes in the system, which are damped on diffusion time scales for small B_{ext} ; however at large B_{ext} , where nonlinear physics plays a role, these undesirable modes can affect the stability of the computations. To avoid difficulties at large B_{ext} , we instead apply the perturbation through a time-dependent boundary condition. Additionally, we note here that the velocity is subject to “no-slip” boundary conditions.

With the Alfvén time in mind, we choose a fixed time step of $dt = 0.689 \tau_A$ at which to evolve the computations to avoid ill-conditioned matrices when solving the implicit systems. We have also run computations with a lower time step, and only found slight quantitative differences in the system’s early-time evolution; they yield the same time-asymptotic state. With this fixed time step, we have run multiple computations varying κ_{divbd} and find that a value of $\kappa_{\text{divbd}} = 7.26 \times 10^{-5} D_{\text{norm}}$ is large enough to control the numerical divergence error with the spatial representation described above.

Figure 1 also shows a (grey) region representing the linear layer of width δ_δ . Nonlinear physics becomes important if the (green) magnetic island resulting from the perturbation field becomes wider than this layer [10]. The linear layer width is set by the local resistivity and viscosity diffusion parameters. The resistivity in a majority of the computations is set to $(\eta/\mu_0) = 2.90 \times 10^{-6} D_{\text{norm}}$, resulting in a Lundquist number $S \equiv \tau_R/\tau_A = 3.45 \times 10^5$, where $\tau_R \equiv a^2/(\eta/\mu_0)$ is the resistive diffusion time based on the half-length of the inflow direction. The value of the isotropic viscosity coefficient is set to $\nu = 2.90 \times 10^{-9} D_{\text{norm}}$ to test the low viscosity model of Ref. [8]; this results in a value for the magnetic Prandtl number $P_m \equiv \tau_R/\tau_V = 10^{-3}$, where $\tau_V \equiv a^2/\nu = 3.45 \times 10^8 \tau_A$ is the viscous diffusion time based on the half-length in the inflow direction. Viscosity is then varied to consider $10^{-3} \leq P_m \leq 1$. This corresponds to the visco-resistive regime of Ref. [16], and is expected to be important for tokamak physics [15]. In the visco-resistive regime, the linear layer width is given by $\delta_\delta = \delta_{\text{VR}} = aS^{-1/3}P_m^{1/6}$, and $\delta_{\text{VR}} = (0.45 - 1.43) \times 10^{-2} L_{\text{norm}}$ for the chosen parameters.

The viscosity coefficient is spatially constant for all linear computations. Nonlinear computations include an edge region where the coefficient is increased as $[1 + (\Delta_{\text{mag}}^{1/2} - 1) \times (|x|/a)^{\Delta_{\text{width}}}]^2$, where $\Delta_{\text{mag}} = 1000$ and $\Delta_{\text{width}} = 5$ yields an edge region that falls to ~ 1 at $|x| \sim a/2$. This additional diffusion avoids unresolved boundary layers while not qualitatively affecting the results, as additional computations have shown.

III. SYSTEM EVOLUTION WITHOUT FLOW

Comparisons of NIMROD computations with the original Hahm and Kulsrud analysis [8] will be considered first. Specifically, we discuss the evolution of nonlinear computations without flow that retain and couple modes $n = 0 - 5$. The equilibrium is perturbed with an $n = 1$ ($k_y a = \pi$) edge magnetic perturbation consistent with

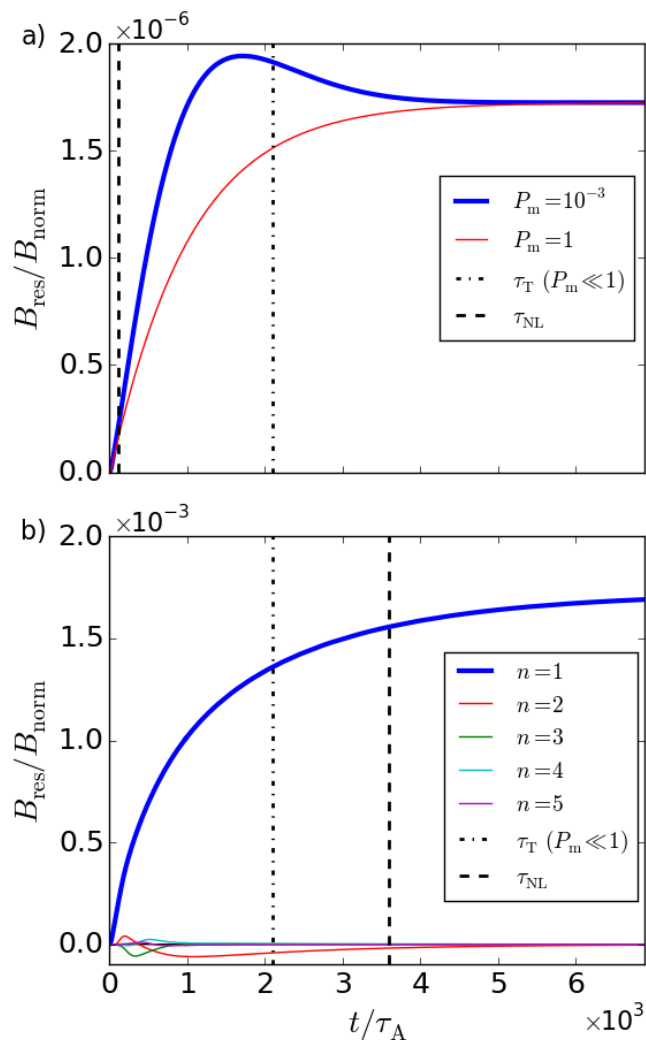


FIG. 3. Nonlinear computations with applied field a) $B_{\text{ext}} = 2 \times 10^{-5} B_{\text{norm}}$ and b) $B_{\text{ext}} = 2 \times 10^{-2} B_{\text{norm}}$. The evolution of the $n = 1$ mode for small applied field exhibits an overshoot, while the evolution of $n = 1$ with the larger applied field monotonically increases, consistent with Ref. [8]. Higher order n modes play a role with larger forcing, implying nonlinear effects are important in this case. This is also evident in the analytical time scales defined by [8], where τ_T is the visco-resistive tearing time and τ_{NL} is a nonlinear “Rutherford-like” time, and nonlinear effects are important for $\tau_T < \tau_{\text{NL}}$.

the phasing shown in Fig. 1. To quantify the evolution of the FMR system, we measure the maximum of the magnetic field B_x on the rational surface at $x = 0$. We refer to this as the “response field” B_{res} as compared to the maximum applied field at the boundary B_{ext} . For zero flow, B_{res} is located at $(x, y) = (0.0, 0.5)a$, in phase with B_{ext} as seen in Eq. (4b).

Figure 3a shows the results from computations with applied field of magnitude $B_{\text{ext}} = 2 \times 10^{-5} B_{\text{norm}}$, where the (thick) blue trace is for a computation with $P_m = 10^{-3}$ and the red trace is with $P_m = 1$. The low-viscosity computation exhibits an overshoot in the response field, qualitatively consistent with the analytical prediction in Ref. [8] as well as computational results in Ref. [60]. The magnitude of the calculated response field is $< 1\%$ differ-

ent from the time-asymptotic analytics of Ref. [8], which predicts

$$B_{\text{res}} = \frac{B_{\text{ext}}}{\cosh(k_y a)} \Rightarrow \frac{B_{\text{ext}}}{\cosh(\pi)}, \quad (7)$$

and yields $B_{\text{res}} = 1.73 \times 10^{-6} B_{\text{norm}}$.

Furthermore, the evolution of the computations follows the analytical predictions in Ref. [8]. For early times before resistivity becomes important in the inertial phase (*i.e.*, $t \ll \tau_{\text{inertial}} \sim \tau_A S^{1/3} = 70.3 \tau_A$) the response field is predicted to evolve as t^2 . Employing a non-linear least squares fitting algorithm on computed results from $t = (10.3 - 24.1) \tau_A$ indicates a time-dependence of $t^{1.85}$. Next, for times after the inertial phase but before the resistive tearing time scale of Ref. [9] (*i.e.*, $\tau_T \sim \tau_A S^{3/5} = 2.10 \times 10^3 \tau_A$ shown as the vertical dashed-dotted lines in Fig. 3) the response field is predicted to evolve as $t^{5/4}$. The computed result from $t = (172 - 207) \tau_A$ exhibits a time-dependence of $t^{1.15}$. Lastly, for times long compared to τ_T the response field is predicted to evolve as $t^{-5/4}$, while computation data from $t = (4830 - 4900) \tau_A$ exhibits a time-dependence of $t^{-1.20}$. Fitting ranges are varied in order to decrease the standard deviation of the fitting parameters to under 1%.

The (red) computation in Fig. 3a with $P_m = 1$ does not exhibit the overshoot seen in the low viscosity computation. The lack of overshoot is qualitatively consistent with computations in Ref. [59] that tested theory in this parameter regime. Physically, the added flow diffusion introduced by viscosity allows a mechanism through which the current layer forming in the inertial phase [8] flattens more rapidly, rather than building up towards a singular response. Since large flows are driven by reconnection in this phase, it is intuitive that viscosity would limit these flows and throttle the reconnection process, ultimately leading to a monotonic temporal increase in the response field.

Figure 3b again uses $P_m = 10^{-3}$, but now the applied $n = 1$ perturbation is increased to $B_{\text{ext}} = 2 \times 10^{-2} B_{\text{norm}}$. The appearance of response fields for $n > 1$ indicates that nonlinear physics is now playing a role, which is consistent with Ref. [8]. The nonlinear island growth is predicted in Ref. [8] to proceed for $\delta_{\text{HK}}/a > S^{-4/5}$ consistent with Ref. [10], which is well satisfied for this perturbation level. Furthermore, the overshoot of the $n = 1$ response has disappeared, again consistent with Ref. [8] that predicted the loss of the overshoot for $\tau_{\text{NL}} \sim (\delta_{\text{HK}}/a)^{1/2} \tau_R > \tau_T$. The nonlinear time τ_{NL} is marked by the vertical dashed lines in Fig. 3; in Fig. 3a the overshoot is apparent for $B_{\text{ext}} = 10^{-5} B_{\text{norm}}$, where $\tau_{\text{NL}} = 1.14 \times 10^2 \tau_A$ is much smaller than τ_T , while in Fig. 3b there is no overshoot for $B_{\text{ext}} = 10^{-2} B_{\text{norm}}$, where $\tau_{\text{NL}} = 3.59 \times 10^3 \tau_A$ is significantly larger than τ_T .

As was the case for the linear-regime computation, the evolution in this nonlinear-regime computation follows the analytical predictions of Ref. [8]. Fitting computation results for times $t = (334 - 420) \tau_A$ (well before τ_{NL}) where theory predicts a time-dependence $\sim t^{2/3}$, computations exhibit evolution as $t^{0.673}$. For times $t = (8570 - 8740) \tau_A$ (long after τ_{NL}) Ref. [8] predicts time-dependence $\sim \tanh^2(t/\tau_{\text{NL}})$, and a fit of the computa-

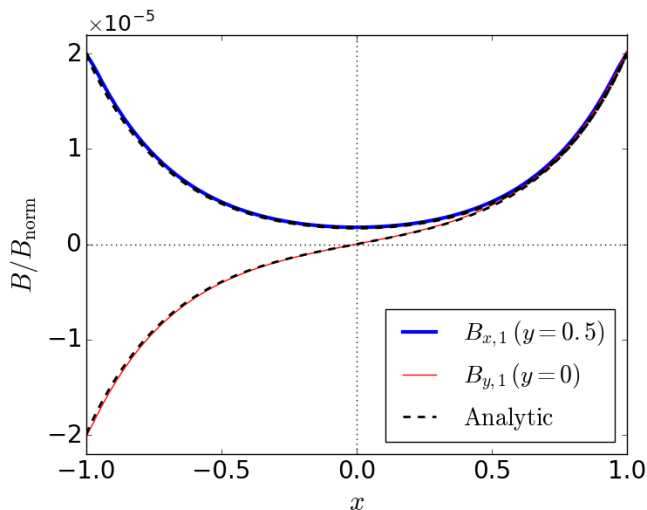


FIG. 4. Time-asymptotic magnetic fields normal (blue) and tangential (red) to the resonant surface for computations with $B_{\text{ext}} = 2 \times 10^{-5} B_{\text{norm}}$ and without flow. These results are consistent with analytical predictions (dashed) of Ref. [8].

tion results also agrees with this prediction, producing $\tau_{\text{NL}} = 2.62 \times 10^3 \tau_A$. Again, the fitting ranges are varied in order to decrease the standard deviation of the fits to under 1%.

In this section, we have shown that NIMROD computations of FMR are consistent with key aspects of the analytical theory developed by Ref. [8]. In the next section, we transition from analysis of the evolution of FMR to that of the time-asymptotic state where we explore the effects of varying diffusion parameters and flow.

IV. LINEAR FLOW SCALING OF RESONANT FIELD IN TIME-ASYMPTOTIC STATE

By extending our computations to times much longer than τ_T , we first examine the time-asymptotic state predictions of Ref. [8]. Translating from the form used in Ref. [8], which used a magnetic scalar potential to describe the fields perpendicular to the guide field ($\mathbf{B}_\perp = \hat{z} \times \nabla \psi$), to the representation of the magnetic perturbation used in the current work, the time-asymptotic magnetic fields are predicted to be

$$B_{x,1}(x) \equiv -\frac{\partial \psi}{\partial y} = B_{\text{ext}} \frac{\cosh(k_y x)}{\cosh(k_y a)} \sin(k_y y), \quad (8a)$$

$$B_{y,1}(x) \equiv \frac{\partial \psi}{\partial x} = B_{\text{ext}} \frac{\sinh(k_y x)}{\cosh(k_y a)} \cos(k_y y). \quad (8b)$$

Results of NIMROD computations alongside these analytical predictions are shown in Fig. 4. The blue and red traces show profiles of $B_{x,1}$ and $B_{y,1}$, respectively, and the dashed lines indicate the excellent agreement with theory.

We next investigate the effect of flowing plasma on the reconnection process. To interpret these results, we adapt the results of the linear, time-asymptotic, cylindrical theory of Ref. [15] to slab geometry. Physically,

a relative flow induces eddy (or Foucault) currents for flow times $L_y/V_{y,0}$ small compared to τ_T , since the non-uniform applied field varies temporally in the reference frame of the resonant surface.

For the linear problem, we first decompose the (total) magnetic flux function into a linear superposition of tearing and “screened” responses $\psi_{\text{tot}} = \psi_T + \psi_S$. Boundary conditions on the tearing component are $\psi_T(|x|=a) = 0$ at the edge of the domain. The boundary conditions on the screened response are that there is no response at the resonant surface $\psi_S(x=0) = 0$ and that the screened response matches the applied field at the edge of the domain $\psi_S(|x|=a) \equiv \psi_{\text{ext}} = \varphi(|x|=a) = B_{\text{ext}}/k_y$.

Since the ψ_{tot} contains information for both the response and applied fields, in order to find a relation between the two, we calculate the jump in the derivative ψ_{tot} in the inflow direction across the resonant surface in the reference frame of the flowing plasma

$$\begin{aligned} a[\partial_x \psi_{\text{tot}}]_0 &= a[\partial_x \psi_T]_0 + a[\partial_x \psi_S]_0 \\ \Rightarrow -i\omega_0 \tau_\delta \psi_{\text{res}} &= a\Delta' \psi_{\text{res}} + a[\partial_x \psi_S]_0. \end{aligned} \quad (9)$$

Here, consistent with Ref. [14], the integral of Faraday’s law across the resonant surface is used to go from the first to the second line, $\partial_x \equiv \partial/\partial x$, $\omega_0 \equiv \vec{k} \cdot \vec{V}_0 = nV_{y,0}/(L_y/2\pi)$ is the initial “slip frequency” characterizing the equilibrium flow frequency at the resonant surface, τ_δ is the linear layer time, which describes the response of the diffusive layer around the resonant surface to the applied field [69], $\psi_{\text{res}} \equiv \psi_{\text{tot}}(x=0)$ is the value of the magnetic flux function at the X-point on the resonant surface, Δ' is the usual stability parameter from [9], and $\cos(k_y y)$ due to the phasing of the applied field has been canceled from each term. Note that the flow $V_{y,0}$ is parallel to the direction of modulation of the applied field, causing the applied field to vary temporally in the reference frame of the moving plasma and generate eddy currents.

To evaluate the jump in $\partial_x \psi_S$, we take the general solution for ψ given by Eq. (7) from [8] and apply the boundary conditions outlined for ψ_{tot} above to find

$$\psi_S(x) = \pm \frac{B_{\text{ext}} \sinh(k_y x)}{k_y \sinh(k_y a)} \cos(k_y y), \quad (10)$$

where the $+(-)$ corresponds to the range $x > 0 (< 0)$. After omitting the $\cos(k_y y)$ as was done in Eq. (9), the jump in ψ_S across the resonant surface is evaluated to be

$$[\partial_x \psi_S]_0 = \frac{2B_{\text{ext}}}{\sinh(k_y a)}. \quad (11)$$

Similarly, Δ' can be found by subtracting Eq. (10) from Eq. (12) in Ref. [8] to give ψ_T , and then evaluating the jump of $\partial_x \psi_T$ to give the tearing-stability parameter as

$$\Delta' = \frac{-2k_y}{\tanh(k_y a)}, \quad (12)$$

consistent with the results from [9] with $k_y a = \pi$, as expected. We likewise define the tearing drive due to the applied external field as

$$\Delta'_{\text{ext}} = \frac{2k_y}{\sinh(k_y a)}. \quad (13)$$

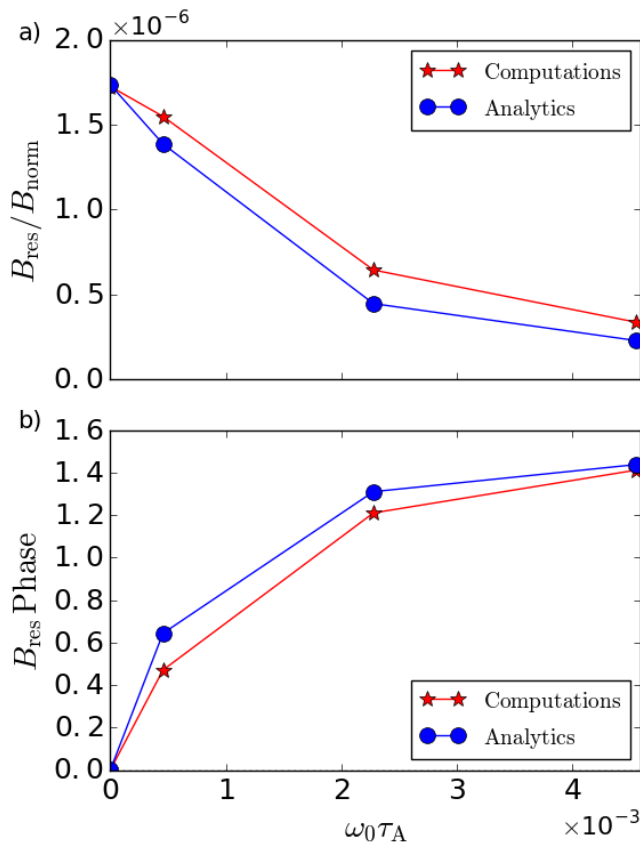


FIG. 5. Parametric scaling of a) reconnected field amplitude and b) phase at the resonant surface as the equilibrium flow along the resonant surface $V_{y,0}$ is varied for a constant applied field of $B_{\text{ext}} = 2 \times 10^{-5} B_{\text{norm}}$. The amplitude characterizes how the reconnected field decreases as the flow is increased. The phase shows the transition from being in phase at $\omega_0 = 0$ toward being completely out of phase as ω_0 is increased. Red data (\star) shows computation results and blue data (\bullet) shows analytic results, which are reasonably consistent.

Both Eqs. (12) and (13) are consistent with those found in Ref. [61]. Rewriting Eq. (9) with Eqs. (10), (12), and (13) and the relation $\psi_{\text{res}} = iB_{\text{res}}/k_y$, yields the relation between B_{ext} and B_{res} as

$$B_{\text{res}} = \frac{a\Delta'_{\text{ext}}}{-a\Delta' - i\omega_0\tau_\delta} B_{\text{ext}}. \quad (14)$$

The dependence on the flow frequency ω_0 is in line with intuition; namely, as ω_0 is increased, oscillatory eddy currents arise to screen out the applied field and the response field at the resonant surface is decreased. Additionally, it is clear that in the limit of no flow with $\omega_0 \rightarrow 0$, Eq. (7) is recovered.

In order to test NIMROD computations with these analytical predictions, we choose a regime of flow and diffusivity in order to define the layer response time τ_δ . The single-fluid, zero- β , non-ideal MHD equations are solved in the vicinity of the resonant surface in Ref. [69], and Ref. [16] shows the four distinct linear response regimes in its Fig. 1. We restrict ourselves here to the *visco-resistive* regime, where the layer response time is given by $\tau_{\text{VR}} = 2.104 \tau_A S^{2/3} P_m^{1/6} = 1.03 \times 10^4 \tau_A$. This regime

is restricted to a flow and resistivity satisfying $Q \equiv \omega_0 \tau_A S^{1/3} < 1$, where Q is the normalized slip frequency, and for viscosity satisfying $Q^{2/3} < P_m < Q^{-3}$. We perform computations having $P_m = 1$ with $Q \leq 0.319$, which corresponds to $\omega_0 \tau_A \leq 4.56 \times 10^{-3}$ for the chosen parameters.

Using the visco-resistive τ_{VR} for τ_δ in Eq. (14), we show a comparison between the resulting analytical prediction and results from NIMROD in Fig. 5. The numerical flow profile $V_{y,0}(x)$ has the form of a Gaussian with width equal to $0.25a$, which nears zero at $|x| = a$ and is relatively flat at the resonant surface. The profile is chosen in order to suppress any unintended effects from flow shear at the resonant surface while satisfying no-slip boundary conditions. Fig. 5a shows B_{res} , where the red data is from NIMROD computations and the blue data corresponds to the analytic prediction with spatially uniform flow. The computation results trend with predictions, though the results are as much as 45% larger than the analytical predictions of the amplitude for the largest flows. Fig. 5b shows the phase of B_{res} relative to B_{ext} . A phase of 0 has the response field spatially aligned with the applied field, and a phase of $\pi/2$ has the fields directly out of phase. As was the case with the amplitude, the computational results show the same trend as the analytical predictions, and are as much as 40% less than predictions.

We note that the discrepancy between the computation and analytic results in Fig. 5 also appears in a recent cylindrical benchmark including NIMROD and M3D-C¹ [70]. In this benchmark, the two codes are found to differ by $\lesssim 4\%$ in computing the amplitude of the reconnected field, and both differ from the analytical prediction by $\lesssim 45\%$. We also mention that the analytic model is derived for the asymptotic visco-resistive parameter regime, which is parametrically isolated from other dissipation regimes [16], while our computations are near the nexus of all dissipation regimes. This may be a significant contributing factor in the variation between our computation results and the analytic predictions.

In a similar fashion to the last section, the NIMROD computations in this section verify key aspects of the analytical model of Ref. [15]. We also note that when we increase the flow, venturing into the *inertial* regime, or increase P_m , venturing into the *visco-inertial* regime, we observe Alfvén resonances [57], as predicted in Ref. [16].

V. NONLINEAR FORCE BALANCE BIFURCATION

In this section, we use the linear treatment of flow scaling from Eq. (14) in the previous section to develop a quasilinear model adapted from the cylindrical geometry model of Ref. [15] for slab geometry. This model is employed to verify nonlinear NIMROD computations, discuss nonlinear computation results of hysteresis in mode penetration and unlocking, and elucidate nonlinear effects on flow scaling of the reconnected field.

A. Time-Asymptotic Nonlinear Force Balance

Here, we are concerned with the time-asymptotic force balance between the two terms on the right-hand side (RHS) of Eq. (1a), the electromagnetic and viscous force densities

$$\mathbf{F}_{\text{EM}} = \mathbf{J} \times \mathbf{B}, \quad (15a)$$

$$\mathbf{F}_{\text{VS}} = -\nabla \cdot \mathbf{\Pi}_i \simeq \nabla \cdot \rho \nu \nabla \Delta \mathbf{V}. \quad (15b)$$

Here, $\Delta \mathbf{V} \equiv \mathbf{V}_0 - \mathbf{V} = -\mathbf{V}_1$ is the deviation of the flow relative to the initial equilibrium flow profile in the reference frame of the flowing plasma. Equation (15b) reflects that local to the resonant surface, it is the viscous force due to the change in the flow that balances the electromagnetic force due to the response magnetic field. Compared to the linear problem discussed in the preceding section, where the initial flow determines the time-asymptotic state, the nonlinear time-asymptotic state depends on the self-consistent flow response to the applied field.

For the present case of a static applied magnetic field with plasma flowing at the resonant surface, the electromagnetic force generates local flow opposite to that of the equilibrium, which self-consistently generates the viscous force that balances with the electromagnetic force. In the following, we denote the onset of mode penetration as the abrupt viscous damping of the flow in the island region.

In order to ascertain the effects of the time-asymptotic force balance, we integrate these force densities over the y dimension and across the dissipative layer at the resonant surface, of width δ_δ , where non-ideal physics allows eddy currents to be driven in and produce an electromagnetic force on the plasma. These integrations yield $\hat{\mathbf{F}}$, the force per unit length in the symmetry direction z , according to

$$\hat{\mathbf{F}} \equiv \int_{-\delta_\delta/2}^{\delta_\delta/2} dx \int_{-L_y/2}^{L_y/2} dy \mathbf{F}. \quad (16)$$

We only consider the \hat{y} -component of $\hat{\mathbf{F}}$ (*i.e.*, $\hat{y} \cdot \hat{\mathbf{F}}$), because only flows parallel to the spatial modulation in the applied field generate eddy currents that generate forces at the resonant surface.

Assuming that the asymmetric $n \neq 0$ responses are described by the linear theory, the electromagnetic force per unit length at the resonant surface is given by

$$\hat{F}_{y,\text{EM}} = \frac{\omega_{\text{res}} \tau_\delta}{(-a\Delta')^2 + (\omega_{\text{res}} \tau_\delta)^2} \frac{\pi n (a\Delta'_{\text{ext}})^2 B_{\text{ext}}^2}{ak_y^2 \mu_0}, \quad (17)$$

where $\omega_{\text{res}} \equiv k_y V_{y,\text{res}}$ is the flow frequency at the resonant surface. The explicit derivation of Eq. (17) is found in Appendix A. We note that this is an $n = 0$ force density due to the $n \neq 0$, quasilinear, quadratic, $\mathbf{J} \times \mathbf{B}$ response. Similarly, the $n = 0$ viscous force density from Appendix B is

$$\hat{F}_{y,\text{VS}} = -\frac{4\pi n \rho \nu(x=0)}{\nu_{\text{int}} a k_y^2} \Delta \omega_{\text{res}}. \quad (18)$$

Here, $\Delta \omega_{\text{res}} \equiv k_y \Delta V_{y,\text{res}} = \omega_0 - \omega_{\text{res}}$ is the flow frequency response at the resonant surface in the reference frame

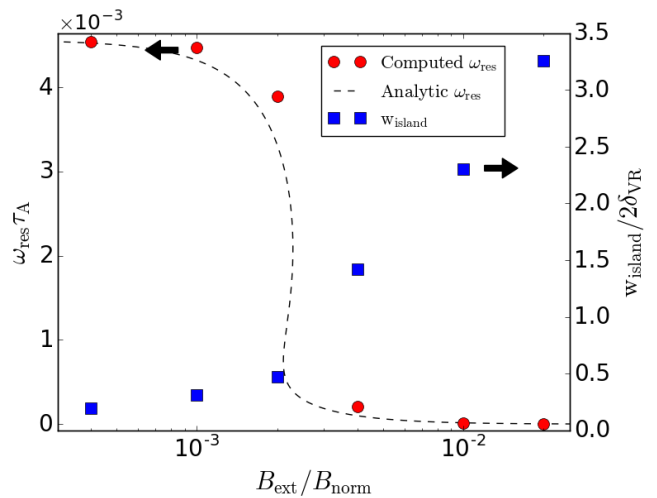


FIG. 6. Nonlinear force balance observed in the time-asymptotic state of computations. The time-asymptotic $\omega_{\text{res}} - B_{\text{ext}}$ computation states given by the red data (solid circles) match the analytical prediction shown by the dashed line and are plotted in reference to the left axis. The time-asymptotic magnetic island width is shown by the blue data (solid boxes) and plotted in reference to the right axis, which is normalized to the visco-resistive linear layer width δ_{VR} .

of the flowing plasma due to the applied field, and ν_{int} is a dimensionless constant corresponding to the effect of the viscosity profile on the flow in the bulk of the plasma for the profile used in NIMROD calculations. For given values of $\Delta_{\text{mag}} = 1000$ and $\Delta_{\text{width}} = 5$, ν_{int} is 0.431.

We now balance these two time-asymptotic, forces per unit length according to $\hat{F}_{y,\text{EM}} + \hat{F}_{y,\text{VS}} = 0$, which results in the relation

$$\frac{\omega_0}{\omega_{\text{res}}} - 1 + \omega_0 \omega_{\text{res}} \tau_\delta'^2 - \omega_{\text{res}}^2 \tau_\delta'^2 = \frac{\nu_{\text{int}} \tau_\delta}{4\rho \nu(x=0)} \left(\frac{\Delta'_{\text{ext}}}{-\Delta'} \right)^2 \frac{B_{\text{ext}}^2}{\mu_0} \equiv A_{\text{RHS}} B_{\text{ext}}^2, \quad (19)$$

where $\tau_\delta' = \tau_\delta / (-a\Delta')$. The solution to this cubic equation for ω_{res} is shown by the dashed line in Fig. 6 for $\omega_0 \tau_A = 4.56 \times 10^{-3}$, $\tau_\delta = \tau_{\text{VR}} = 1.03 \times 10^4 \tau_A$ in the visco-resistive dissipative regime with $S = 3.45 \times 10^5$ and $P_m = 1$, and an $n = 1$ applied perturbation field. We refer to this solution in $\omega_{\text{res}} - B_{\text{ext}}$ space as a “response curve”.

The time-asymptotic flow at the resonant surface ω_{res} is plotted as a function of the applied field magnitude B_{ext} in Fig. 6. As the applied field is increased, the time-asymptotic state bifurcates from a high-slip state with a small island and little viscous damping of flow to a low-slip state with a large island and viscous damping that dramatically slows the flow at the resonant surface. For the parameters chosen in these calculations, the island in the low-slip state exceeds the linear layer width $2\delta_{\text{VR}} = 2.86 \times 10^{-2} L_{\text{norm}}$. As such, the linear theory used to obtain Eq. (17) is not valid and a modified Rutherford magnetic island theory is needed. Nonetheless, the force balance relation Eq. (19) is a useful expression for interpreting the numerical results. Analytically, the solution

to Eq. (19) exhibits a bifurcation when its derivative with respect to ω_{res} has non-degenerate, real roots. Physically, this condition occurs when the initial flow frequency ω_0 is above a critical threshold given by

$$\omega_0 > \omega_{0,\text{crit}} = \frac{3\sqrt{3}}{\tau'_\delta}, \quad (20)$$

which is marginally satisfied for the system parameters chosen in these computations. Note that $\omega_{0,\text{crit}}$ only depends on S , P_m , and Δ' ; thus the initial flow frequency at which a bifurcation can occur is independent of the applied field.

Nonlinear computations with NIMROD are within a factor of 2 of the quasilinear predictions of Eq. (19) at the poorest agreement for the largest applied field and within 0.5% at the best agreement, as shown by the red dots in Fig. 6. Also shown are the full widths of FMR islands consistent with

$$w_{\text{island}} \equiv 4 \sqrt{\frac{aB_{\text{res}}}{k_y B_{y,0}(x=a)}} \quad (21)$$

by the blue dots.

Direct evaluation of the simulated FMR islands are also in good agreement with the predictions based on Eq. (21). Shown in Fig. 7 are Poincaré plots of computations with a) $B_{\text{ext}} = 2 \times 10^{-3} B_{\text{norm}}$ and b) $B_{\text{ext}} = 4 \times 10^{-3} B_{\text{norm}}$, where the red lines trace the approximate location of the island separatrix (the exact location of the separatrix is slightly inside). These Poincaré plots have seed points along $y = -1$, and only contours near the separatrix are shown. The magnetic island widths are measured at their widest, differing from predictions by 3.3% for $B_{\text{ext}} = 4 \times 10^{-3} B_{\text{norm}}$ and 15.9% for $B_{\text{ext}} = 2 \times 10^{-3} B_{\text{norm}}$.

The smaller applied perturbation results in a time-asymptotic state exhibiting a high-slip, field-screened configuration with a thin FMR island, while a marginally larger applied field results in a low-slip, mode-penetrated configuration with a wide FMR island. The quasilinear physics contained in Eq. (19) allows for significant viscous flow damping as the applied field is increased through a threshold value at $B_{\text{ext}} = 2.29 \times 10^{-3} B_{\text{norm}}$, which leads to mode penetration. The high-slip state in Fig. 7 has a magnetic island that is out of phase with the applied field, as observed by the X-point being displaced from $y = 0$, shown by the dotted line. The low-slip state is only slightly out of phase since ω_{res} is small but still finite as seen in Fig. 6.

B. Hysteresis of Mode Penetration and Unlocking

Close inspection of the response curve and the associated time-asymptotic numerical results in Fig. 6 reveals that for a finite range of applied field [$B_{\text{ext}} = (2.11 - 2.29) \times 10^{-3} B_{\text{norm}}$], there exists three possible values of ω_{res} at a single value of B_{ext} which satisfy Eq. (19). For these values of applied field, the flow frequency at the time-asymptotic state is dependent on the history of the

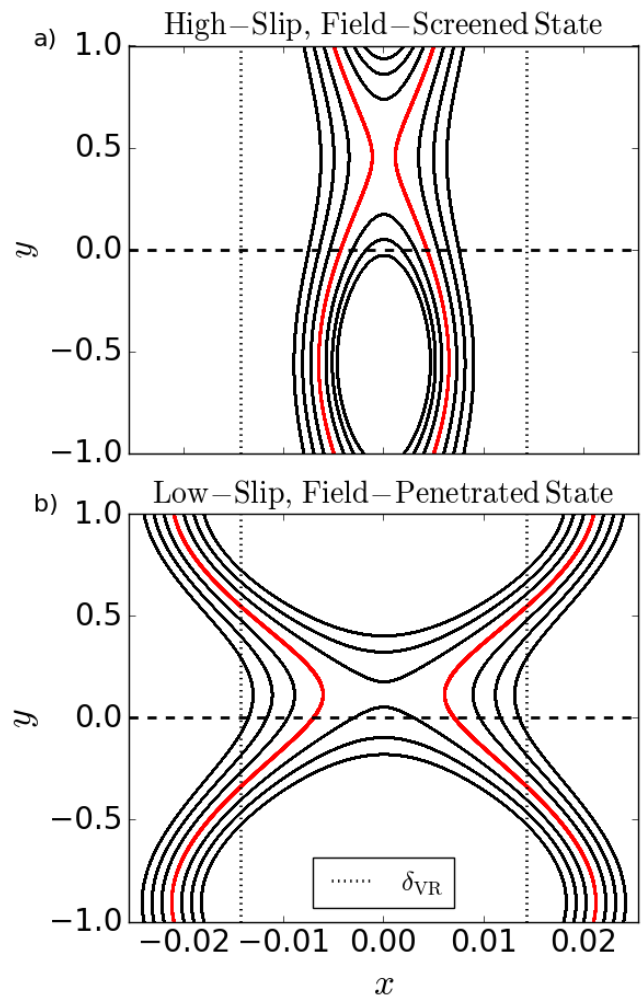


FIG. 7. Poincaré plots of the magnetic field structure in time-asymptotic states shown in Fig. 6 of nonlinear computations with applied field a) $B_{\text{ext}} = 2 \times 10^{-3} B_{\text{norm}}$ and b) $B_{\text{ext}} = 4 \times 10^{-3} B_{\text{norm}}$. The top plot is consistent with a time-asymptotic high-slip state having a small magnetic island and the bottom plot a low-slip state having a large island, indicated by the red contours in each plot.

system, *i.e.*, the system exhibits hysteresis. If the applied field is increased from a value below the threshold for multiple flow frequency roots, the time-asymptotic state is on the high-slip branch; but if the applied field is decreased from a value above the threshold, a low-slip state is realized for the same time-asymptotic applied field. We note that the intermediate flow frequency root is unstable and relaxes to either the high or low-slip root when perturbed.

Beginning in the high-slip state, mode penetration occurs when the applied field is increased through the upper extent of the range with multiple flow frequency roots, and the time-asymptotic state undergoes a transition from the high-slip state to the low-slip state. We refer to the critical applied field needed for mode penetration as $B_{\text{ext,pen}}$. For a system in the visco-resistive dissipation regime, which satisfies Eq. (20) and exhibits a bifurcation, Ref. [16] states that $B_{\text{ext,pen}}$ is equal to the applied field consistent with $\omega_{\text{res}} = \omega_0/2$ in Eq. (19). Substitut-

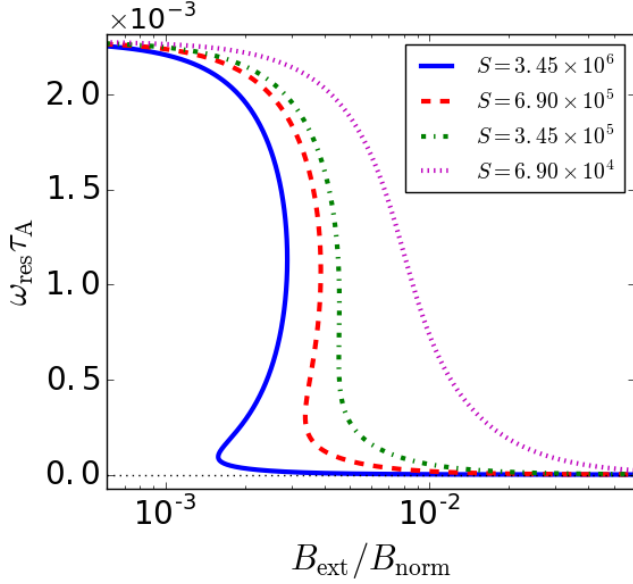


FIG. 8. Solutions of Eq. (19) plotted for different values of S , where the initial flow frequency is kept constant at a value of $\omega_0 \tau_A = 2.28 \times 10^{-3}$. Higher S corresponds to a lower $\omega_{0,\text{crit}}$. For values of S where $\omega_{0,\text{crit}} < \omega_0$, the system exhibits hysteresis. The series of curves show that the range between $B_{\text{ext,pen}}$ and $B_{\text{ext,unlock}}$ increases as S increases. Hysteresis is lost for lower S , which has a larger $\omega_{0,\text{crit}}$.

TABLE I. Characteristic parameter values used in force balance bifurcation calculation of Eq. (19) that are plotted in Fig. 8. With $\omega_0 \tau_A = 2.28 \times 10^{-3}$ and $P_m = 10$ held constant, $\omega_{0,\text{crit}}$ is found for different values of S . The normalized flow frequency Q is seen to stay below unity for all S , which excludes Alfvén resonances.

$S(\times 10^5)$	0.690	3.45	6.90	34.5
$\omega_{0,\text{crit}} \tau_A (\times 10^{-3})$	6.13	2.16	1.36	0.465
Q_0	0.093	0.159	0.201	0.344

ing $\omega_{\text{res}} = \omega_0/2$ into Eq. (19) results in the relation

$$B_{\text{ext,pen}}(\omega_0) = \frac{1}{2} \sqrt{\frac{4 + \omega_0^2 \tau_\delta'^2}{A_{\text{RHS}}}}. \quad (22)$$

For the system parameters in Fig. 6, Eq. (22) yields $B_{\text{ext,pen}} = 2.29 \times 10^{-3} B_{\text{norm}}$ which agrees with the numerical solution of Eq. (19).

Similarly, beginning in the low slip state, mode unlocking occurs when the applied field is decreased through $B_{\text{ext,unlock}}$, at the lower extent of the range of multiple flow frequency roots, and the system undergoes a transition from a low-slip to high-slip time-asymptotic state. For the system parameters shown in Fig. 6, the numerical solution of Eq. (19) yields $B_{\text{ext,unlock}} = 2.11 \times 10^{-3} B_{\text{norm}}$.

We can increase the range between $B_{\text{ext,pen}}$ and $B_{\text{ext,unlock}}$ by increasing ω_0 . However, as ω_0 is increased, the normalized flow frequency $Q_0 = \tau_A S^{1/3} \omega_0$ must be kept less than unity to stay in the visco-resistive regime and avoid Alfvén resonances [16]. The computations in Fig. 6 already have $Q_0 = 0.319$, and increasing ω_0 by only a factor of two leads to the onset of Alfvén resonances.

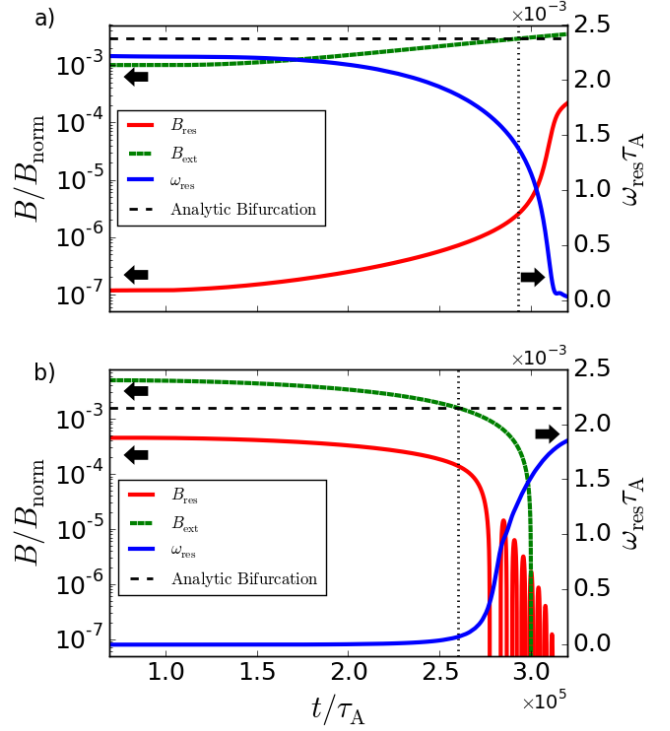


FIG. 9. For the computation parameters characterizing the blue response curve in Fig. 8, we employ a time-dependent applied field (described in text) to induce both a) mode penetration and b) unlocking transitions. The mode penetration transition increases the time-dependent applied field through $B_{\text{ext,pen}}$, where the unlocking transition decreases the applied field through $B_{\text{ext,unlock}}$. The dashed green lines indicate the applied field B_{ext} , the red lines indicate the response field B_{res} , and the blue lines indicate the flow frequency at the resonant surface ω_{res} . The vertical dotted lines indicate the time when the applied field crosses the critical threshold determined from analytic predictions, as shown by the horizontal dashed lines.

Thus, in order to have $\omega_0 \gg \omega_{0,\text{crit}}$ in addition to $Q_0 \ll 1$ for strong hysteresis, system parameters are chosen to be $S = 3.45 \times 10^6$ and $\omega_0 \tau_A = 2.28 \times 10^{-3}$. Additionally, we choose $P_m = 10$, allowing for a larger viscous force and thus rapid flow response. The hysteresis is accentuated for these values, as can be seen by the response curve plotted as the (solid) blue line in Fig. 8. The other traces in this plot correspond to lower Lundquist numbers, and it is evident that these conditions inhibit hysteresis effects. The characteristic parameters for these response curves are given in Table I.

Figure 9 reproduces the hysteresis for the $S = 3.45 \times 10^6$ case in Fig. 8. Computations begin by ramping the applied magnetic field (not shown in Fig. 9) with a time-dependence of $B_{x,1}(|x| = a, y, t) = B_{\text{ext}} \sin(k_y y)(1 - e^{-t/\tau_{\text{ext}}})$, where $\tau_{\text{ext}} = 69.0 \tau_A$ was chosen to be long compared to the Alfvén time. This time-dependence is employed until B_{res} reaches a steady-state, quantified by where the transient variation in the reconnected field decreases to less than 1% of the total reconnected field.

From Eq. (22) we find a value of $B_{\text{ext,pen}} = 2.89 \times 10^{-3} B_{\text{norm}}$ is needed to trigger a mode penetration tran-

sition as the applied field is increased, and from Eq. (19) we find a value of $B_{\text{ext,unlock}} = 1.58 \times 10^{-3} B_{\text{norm}}$ is needed for an unlocking transition as the applied field is decreased. Thus, to observe mode penetration we initiate one computation with $B_{\text{ext}} = 10^{-3} B_{\text{norm}} < B_{\text{ext,pen}}$, and to observe unlocking we initialize a second computation with $B_{\text{ext}} = 5 \times 10^{-3} B_{\text{norm}} > B_{\text{ext,pen}} > B_{\text{ext,unlock}}$. The steady-state computation parameters can be seen to the left of the plots in Fig. 9, where Fig. 9a exhibits mode penetration and Fig. 9b exhibits unlocking. The dashed green traces indicate B_{ext} , the red traces B_{res} , and the blue traces ω_{res} .

Once steady-state has been reached, the time-dependent field evolution is replaced with $B_{x,1}(|x| = a, t) = B_{\text{ext}} \{1 \pm [(t - t_{\text{ss}})/\tau_{\text{ext}}] \tanh[(t - t_{\text{ss}})/\tau_{\text{ext}}]\}$. Here, $+$ ($-$) indicates the profile employed for mode penetration (unlocking), t_{ss} is the time when a steady-state is attained, and $\tau_{\text{ext}} = 1.38(5.17) \times 10^4 \tau_{\text{A}}$ characterizes the very gradual change in the applied field employed for mode penetration (unlocking) to elucidate the hysteresis.

The evolution of the applied field, reconnected field, and flow frequency can be observed in Fig. 9. We note that B_{res} in Fig. 9b is the value of the reconnected field at $(x, y) = (0.0, 0.5)$ rather than the maximum reconnected field as in preceding figures. As the external field is increased (decreased) through the threshold $B_{\text{ext,pen(unlock)}}$, indicated by the horizontal dashed line in each plot, the reconnected field is observed to increase (decrease), undergoing mode penetration (unlocking), and is accompanied by a sharp decrease (increase) in the flow frequency. The vertical dotted lines indicate the times at which the mode penetration and unlocking threshold applied fields are reached.

Another feature of unlocking shown in Fig. 9 is the oscillation of B_{res} with decreasing magnitude. This dynamics can be understood by observing the series of Poincaré plots in Fig. 10. As time increases and the unlocking bifurcation proceeds, the magnetic island shrinks, consistent with decreasing magnitude of B_{res} in Fig. 9. More importantly though, Fig. 10 reveals that the previously locked island is convecting in the $+y$ direction, unlocked from the externally applied field, consistent with predictions in Ref. [15]. The flow frequency of the convecting island increases monotonically after unlocking, and is $\omega_{\text{unlocked}}\tau_{\text{A}} = 1.85 \times 10^{-3}$ at $t = 3.21 \times 10^5 \tau_{\text{A}}$. Additionally, the Poincaré plot in c) is observed to have a smaller magnetic island than that in d); in c) the mode is nearly π out of phase with the externally applied field, which compresses the magnetic island.

C. Nonlinear Flow Scaling of Resonant Field in Time-Asymptotic State

Thus far in this section, we have demonstrated that computational results from NIMROD agree well with predictions from quasilinear analytic theory for force balance. We conclude this section by exploring how nonlinear force balance affects flow scaling of the resonant field and contrasting results from nonlinear computations

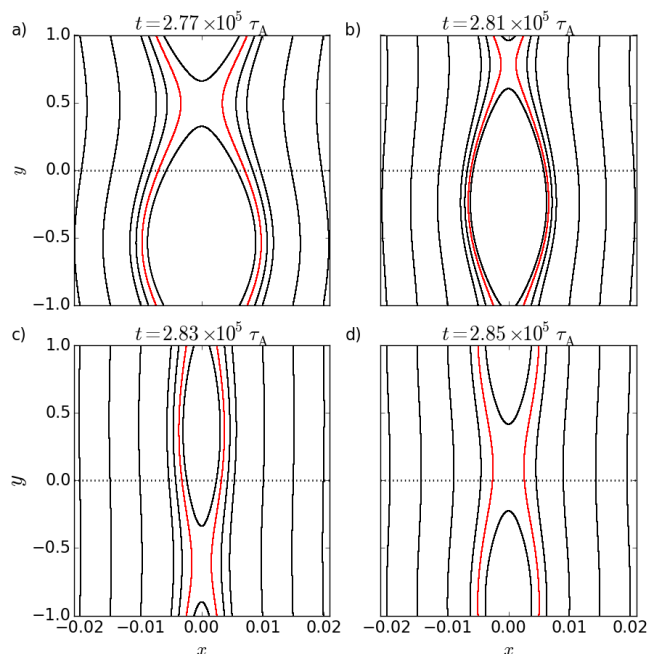


FIG. 10. Poincaré plots of the magnetic field structure after the unlocking transition shown in Fig. 9b. The individual plots a) - d) correspond to evolution in time, where the former mode-penetrated magnetic island has unlocked from the externally applied field and is convecting in the positive y direction. Because the reconnected field is decreasing during this time, the island width is observed to decrease also. Additionally, when the island is out of phase with the external field, there is an extra reduction in island width, observed in c).

against linear computational results similar to those discussed in section IV.

Figure 11 shows a series of normalized response curves where the initial flow frequency is varied, while keeping all other system parameters constant at the values specified in section IIB. Figure 11a clearly shows that as the initial flow frequency ω_0 is increased above $\omega_{0,\text{crit}}\tau'_{\text{VR}} = 3\sqrt{3}$ the system exhibits hysteresis. Additionally, it is clear from Fig. 11b that the time-asymptotic flow frequency ω_{res} decreases below ω_0 as B_{ext} is increased from zero. At large values of B_{ext} , there is a transition from a high-slip to a low-slip state. The transition is gradual for $\omega_0 < \omega_{0,\text{crit}}$, but abrupt for $\omega_0 > \omega_{0,\text{crit}}$ due to the existence of a bifurcation.

The decrease in ω_{res} is better appreciated by factoring the left-hand side of the quasilinear force-balance Eq. (19) as

$$\left(\frac{\omega_0}{\omega_{\text{res}}} - 1\right)(1 + \omega_{\text{res}}^2 \tau_{\text{VR}}'^2) = A_{\text{RHS}} B_{\text{ext}}^2. \quad (23)$$

Because the RHS and the second factor in parentheses on the left-hand side (LHS) of Eq. (23) are > 0 , $\omega_0/\omega_{\text{res}}$ must increase from unity as the RHS increases from 0. In addition to the proportionality of the RHS of Eq. (23) to the square of the applied field, it also depends through the A_{RHS} factor defined in Eq. (19) on the equilibrium configuration through $[\Delta'_{\text{ext}}/(-\Delta')^2]$ and the dissipation

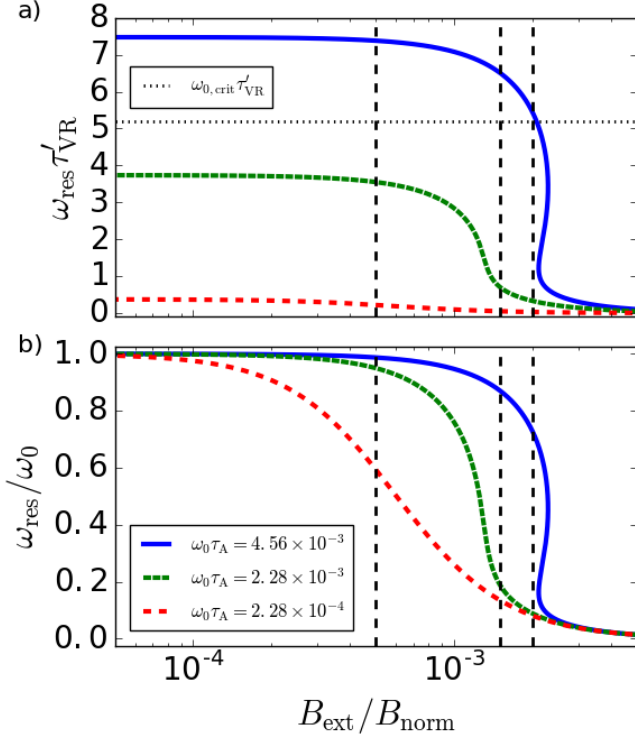


FIG. 11. Solutions for ω_{res} from Eq. (19), which are plotted for different values of $\omega_0 \tau_A$ and normalized by a) $\omega_{\text{res}} \tau'_{\text{VR}}$ and b) $\omega_{\text{res}} / \omega_0$. Solutions exhibit hysteresis for $\omega_0 \tau'_{\text{VR}} > \omega_{0, \text{crit}} \tau'_{\text{VR}} = 3\sqrt{3}$, as seen in a). Note that ω_0 , found in the limit of $B_{\text{ext}} \rightarrow 0$, differs from ω_{res} as B_{ext} is increased through the transition region, as seen for different values of $\omega_0 \tau_A$ in b). Vertical dashed lines correspond to values of external forcing examined in Fig. 12.

through $\nu(x=0)/\nu_{\text{int}}$ and $\tau_{\text{VR}} \sim S^{2/3}$. Furthermore, the magnitude of $\omega_0 / \omega_{\text{res}}$ also depends self-consistently on ω_{res} through the second factor on the LHS of Eq. (23). This analysis is consistent with the decrease of $\omega_{\text{res}} / \omega_0$ observed in Figs. 8 and 11 as B_{ext} is increased.

The flow response (*i.e.*, $\omega_{\text{res}} / \omega_0 < 1$) is due to the viscous damping required for quasilinear force balance. Because the quasilinear force balance affects the flow frequency of the time-asymptotic state, Eq. (14) for the reconnected field should be evaluated using ω_{res} from Eq. (19) or Eq. (23) rather than ω_0 . Rewriting Eq. (14) to reflect this interpretation yields

$$B_{\text{res}} = \frac{a \Delta'_{\text{ext}}}{-a \Delta' - i \omega_{\text{res}} \tau_{\delta}} B_{\text{ext}}. \quad (24)$$

Equation (23) and Fig. 11 show that the nonlinear flow response ω_{res} used to determine the scaling of B_{res} in Eq. (24) depends on both ω_0 and B_{ext} , rather than just the initial flow frequency as was the case for the linear problem.

In Fig. 12, we illustrate how B_{res} with nonlinear flow scaling differs from linear flow scaling, as a function of initial flow frequency and applied field. The three plots correspond to the different values of external forcing indicated by the vertical dashed lines in Fig. 11. Dashed traces in Fig. 12 correspond to (wide-spaced blue) linear

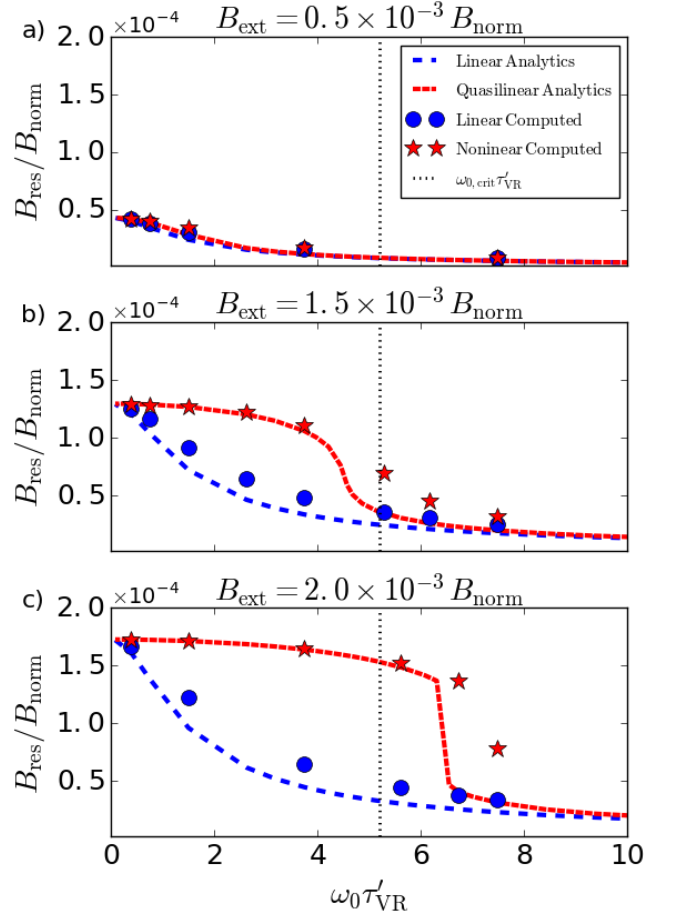


FIG. 12. Comparison between linear (blue data) and nonlinear (red data) analytic theory (dashed lines) and computation results (circles and stars) for a parametric scan of initial flow frequency. The applied magnetic field varies between the plots, where the field magnitudes are indicated by the vertical dashed lines in Fig. 11. Nonlinear results exhibit increased reconnection compared to the linear results. A discontinuous transition from a low-slip to a high-slip state is observed in c), where $B_{\text{ext}} > B_{\text{ext, pen}}(\omega_{0, \text{crit}}) = 1.65 \times 10^{-3} B_{\text{norm}}$.

and (narrow-spaced red) quasilinear analytical predictions, which only display the high-slip solution if a system exhibits a bifurcation. The blue traces are the solution of Eq. (14) for a parametric scan of ω_0 , and the red traces use the same parametric scan of ω_0 in Eq. (19) to find ω_{res} , which is then used in Eq. (24). Time-asymptotic NIMROD computation results are plotted over the analytic predictions with (blue) circles for linear computations and (red) stars for nonlinear computations.

Figure 12 demonstrates that as B_{ext} is increased, the nonlinear computations exhibit increased reconnection compared to the linear computations. This is because nonlinear computations transition to a low-slip state, which allows for additional field to reconnect. As the initial flow is increased beyond the vertical dotted lines indicating where $\omega_0 \tau'_{\text{VR}} = \omega_{0, \text{crit}} \tau'_{\text{VR}}$, the FMR systems exhibit bifurcation. For $\omega_0 = \omega_{0, \text{crit}}$, Eq. (22) yields a field $B_{\text{ext, pen}}(\omega_{0, \text{crit}}) = 1.65 \times 10^{-3} B_{\text{norm}}$. For the applied fields in Figs. 12a and b where $B_{\text{ext}} < B_{\text{ext, pen}}(\omega_{0, \text{crit}})$,

the quasilinear analytics predict a smooth transition of the amount of reconnection from low-slip states at small ω_0 to high-slip states at large ω_0 . However, in Fig. 12c where $B_{\text{ext}} > B_{\text{ext,pen}}(\omega_{0,\text{crit}})$, the transition from low-slip to high-slip exhibits a discontinuity. Thus, the condition in which quasilinear flow scaling predicts a discontinuous transition is given by

$$B_{\text{ext}} > B_{\text{ext,pen}}(\omega_{0,\text{crit}}). \quad (25)$$

As was the case for computation data in section IV, the magnitude of the linear response computations trend well with predictions, but are $\lesssim 48\%$ over predictions for the largest flows. However, while the nonlinear computation data exhibit increased reconnection as B_{ext} is increased, which agrees with the quasilinear analytical predictions, the series of computations satisfying Eq. (25) do not show a clear discontinuous jump from a low-slip to a high-slip state. The deviation from the predictions for this series of computations is up to a factor of ~ 2.2 different. This discrepancy is understandable because Eq. (14) is derived for the asymptotic visco-resistive parameter regime, while our computations approach the nexus of multiple dissipation regimes as ω_0 is increased.

VI. CONCLUSIONS AND DISCUSSION

In this work, we study forced magnetic reconnection in slab geometry with flows using the NIMROD code to evolve the visco-resistive MHD equations. Taylor's problem is initialized by implementing a magnetic perturbation in an edge region of the computational domain, consistent with the analytical boundary displacement perturbation of Ref. [8].

We verify this computational setup with the analytical predictions of evolution in Ref. [8]. We find excellent quantitative agreement with the observation of overshoot in the FMR for small amplitude perturbations in a low viscosity system. Furthermore, we find favorable quantitative agreement when fitting computational data to analytical predictions of the evolution from Ref. [8]. We also verify that NIMROD computes the time-asymptotic state predicted by Ref. [8].

With confidence in the numerically computed time-asymptotic states, we derive linear flow screening relations in the slab geometry similar to those in Ref. [15] for the cylindrical geometry. We then test these analytical predictions and find that they are in good agreement with linear computations for both the magnitude of the reconnected field at the resonant surface and the spatial (phase) shift of the response field relative to the externally applied field.

The linear flow scaling results are then applied to develop a quasilinear formulation of force balance in slab geometry similar to that in Ref. [15] for cylindrical geometry. We show that the analytic theory predicts a bifurcation in the flow frequency at the resonant surface, which leads to a transition from a high-slip, flow-screened state to a low-slip, mode-penetrated state as the externally applied field is increased through a critical threshold. This force balance bifurcation is borne out in time-asymptotic

NIMROD computations, and Poincaré plots show the FMR island structure in the two branches. While we found good agreement between our quasilinear analytical and computational results, we again note that when w_{island} exceeds the linear layer width, the electromagnetic force should be derived with a modified Rutherford equation.

In addition to the linear and nonlinear code verification work, we also discuss several novel results from nonlinear mode penetration computations. First, we employ a time-dependent applied field in order to directly characterize the hysteresis of the nonlinear force balance bifurcation. We find that the magnitude of external forcing needed for mode penetration, which produces a large, locked island, and unlocking of the island are different. Both are consistent with our analytical predictions. Furthermore, we observe that the unlocking process is accompanied by convection of the formerly locked island, which rotates independently from the externally applied field. Lastly, we contrast linear and nonlinear results for flow scaling analytics and computations, and find that as the external forcing is increased toward the magnitude of the critical field needed for mode penetration, the nonlinear B_{res} response increases from the linear results due to the nonlinear flow response, consistent with equilibrium balance of the viscous and electromagnetic forces.

Computational evidence of a convecting nonlinear magnetic island after the unlocking bifurcation in Figs. 9b and 10 is potentially relevant to experimental results. These computation observations are reminiscent of experimental results presented in Fig. 5 of Ref. [28], where an $n = 1$ mode was observed to unlock towards the end of an ELM suppressed state and rotate with decreasing magnitude during the back-transition to conditions favorable to ELMs. While the applied field was $n = 2$ in Ref. [28], the similarities to the present nonlinear effects in Fig. 9b and Fig. 10 are striking, and future numerical and experimental studies should address physics of the unlocking bifurcation.

Another interesting result of the present study, which is pertinent for understanding recent experimental observations, is that the scaling of B_{res} with the quasilinear-determined flow differs significantly from that with linear flow scaling. Recent studies of the ITER baseline scenario in DIII-D [31] demonstrate that at the low rotations predicted for ITER, the RMPs used to suppress ELMs trigger 2/1 tearing modes. Linear modeling has shown a discrepancy with the experimental magnetic response, and it is hypothesized that nonlinear FMR bifurcation physics may be important. While a proper analysis of flow scaling in a tokamak plasma must take into account realistic geometry and physical effects, nonlinear physics becomes significantly important even below the B_{ext} required for a discontinuous transition given in Eqs. (22) and (25).

We conclude by again emphasizing the importance of nonlinear, extended-MHD modeling for understanding FMR processes in tokamaks to address the effects of RMPs on ELMs. The present study verifies that the NIMROD code is well-suited to investigate FMR in slab geometry, and future work aims to apply its methods

towards understanding FMR in more complex geometrical and physical systems. The future use of codes employing these models is also important for understanding macro-scale physics and verifying predictive models, such as Ref. [29], which describes observations of H-mode pedestal ELM suppression due to the application of RMPs. The verification and validation of these generalized models are of critical importance to the successful operation of ITER.

Data used to generate figures can be obtained in digital format by following the link in Ref. [71].

ACKNOWLEDGMENTS

The first author would like to thank E. Howell, K. Bunkers, B. Cornille, and T. Bechtel for helpful discussions related to computation and visualization with NIMROD, and A. Becerra and D. Brennan for insightful discussion on underlying FMR physics. All the authors thank R. Nazikian for his experimentalist's perspective and motivation for these FMR studies.

This research was supported in part by the U. S. Department of Energy (DOE), Office of Science, Office of Fusion Energy Sciences under grants DE-FG02-92ER54139 and DE-FG02-86ER53218. The first author was also supported in part by the U. S. DOE Fusion Energy Sciences Postdoctoral Research Program administered by the Oak Ridge Institute for Science and Education (ORISE) for the DOE. ORISE is managed by Oak Ridge Associated Universities (ORAU) under DOE contract number DE-SC0014664. All opinions expressed in this paper are the authors' and do not necessarily reflect the policies and views of DOE, ORAU, or ORISE.

Appendix A: Electromagnetic Force Derivation

In this appendix we derive the the \hat{y} component of the electromagnetic force per unit length in the z direction within a layer of width δ_δ about the resonant surface at $x = 0$ in the slab geometry. This derivation follows the same general procedure as in Ref. [15] for the slab geometry instead of the cylindrical geometry, and includes greater detail.

By applying the definition in Eq. (16) of the force per unit length to the \hat{y} component of the electromagnetic force density in Eq. (15a), and assuming $J_z \gg J_\perp$, we find

$$\hat{F}_{y,\text{EM}} = \int_{-\delta_\delta/2}^{\delta_\delta/2} dx \int_{-L_y/2}^{L_y/2} dy (J_z B_x). \quad (\text{A1})$$

With $B_{x,0} = 0$, $B_{x,1} = B_{n=1} e^{ik_y y} + B_{n=1}^* e^{-ik_y y}$, and $J_z = J_{z,0} + J_{z,n=0} + \sum_{n=1} [J_{z,n} e^{ik_y(n)y} + J_{z,n}^* e^{-ik_y(n)y}]$, Eq. (A1) becomes

$$\hat{F}_{y,\text{EM}} = L_y \int_{-\delta_\delta/2}^{\delta_\delta} dx (J_{z,n=1} B_{x,n=1}^* + J_{z,n=1}^* B_{x,n=1}). \quad (\text{A2})$$

Next, we recall that the in-plane magnetic field perturbation can be represented by a scalar flux function as $\mathbf{B}_{\perp,1} = \hat{z} \times \nabla \psi$, giving $J_{z,1} = (1/\mu_0) \nabla^2 \psi = (\partial_x^2 - k_y^2) \psi$. We can rewrite Eq. (A2) as

$$\hat{F}_{y,\text{EM}} = \frac{ik_y L_y}{\mu_0} \int_{-\delta_\delta/2}^{\delta_\delta/2} dx [\psi^* \partial_x^2 \psi - \psi \partial_x^2 \psi^*], \quad (\text{A3})$$

which simplifies to

$$\hat{F}_{y,\text{EM}} = \frac{-2k_y L_y}{\mu_0} \int_{-\delta_\delta/2}^{\delta_\delta/2} dx \text{Im}[\psi^* \partial_x^2 \psi]. \quad (\text{A4})$$

Next, integrating by parts yields

$$\hat{F}_{y,\text{EM}} = \frac{-2k_y L_y}{\mu_0} \text{Im}(\psi^* \partial_x \psi) \Big|_{-\delta_\delta/2}^{\delta_\delta/2}. \quad (\text{A5})$$

We now apply the same substitution as in Eq. (9) to obtain

$$\hat{F}_{y,\text{EM}} = \frac{-2k_y L_y}{a\mu_0} \text{Im}(-i\omega\tau_\delta |\psi_{\text{res}}|^2). \quad (\text{A6})$$

Following this substitution, we use the relation $\psi_{\text{res}} = iB_{\text{res}}/k_y$ and Eq. (14) to write the force per unit length of the \hat{y} component of the electromagnetic force in the linear layer as

$$\hat{F}_{y,\text{EM}} = \frac{L_y}{2ak_y} \frac{\omega\tau_\delta}{(-a\Delta')^2 + (\omega\tau_\delta)^2} (a\Delta'_{\text{ext}})^2 \frac{B_{\text{ext}}^2}{\mu_0}, \quad (\text{A7})$$

where an additional factor of 1/4 is included because Eq. (14) is derived for $B_{x,1} = B_{\text{ext}} \sin(k_y y)$, rather than $B_{x,1} = 2B_{n=1} \sin(k_y y)$ as in Eq. (A2). Lastly, since we know that $L_y = 2\pi n/k_y$, this relation can be written as

$$\hat{F}_{y,\text{EM}} = \frac{\omega\tau_\delta}{(-a\Delta')^2 + (\omega\tau_\delta)^2} \frac{\pi n (a\Delta'_{\text{ext}})^2}{ak_y^2} \frac{B_{\text{ext}}^2}{\mu_0}. \quad (\text{A8})$$

Appendix B: Viscous Force Derivation

In this appendix we derive the \hat{y} component of the viscous force per unit length in the z direction within a layer of width δ_δ about the resonant surface at $x = 0$ in the slab geometry. This derivation follows the same general procedure as in Ref. [15], but for the slab geometry instead of the cylindrical geometry.

By applying the definition in Eq. (16) of the force per unit length to the \hat{y} component of the viscous force density in Eq. (15b), we begin with

$$\hat{F}_{y,\text{VS}} = \int_{-\delta_\delta/2}^{\delta_\delta/2} dx \int_{-L_y/2}^{L_y/2} dy [\partial_x(\rho\nu\partial_x\Delta V_y) + \partial_y(\rho\nu\partial_y\Delta V_y) + \partial_z(\rho\nu\partial_z\Delta V_y)]. \quad (\text{B1})$$

Because $\Delta V_y = -V_{y,1} = -V_{y,n=0} - \sum_{n=1} [V_{y,n} e^{ik_y y} + V_{y,n} e^{-ik_y y}]$, only the $n = 0$ term makes it through the y integration and $\partial_y \rightarrow 0$. Also since z is a symmetry direction, $\partial_z \rightarrow 0$. This simplifies Eq. (B1) to

$$\begin{aligned} \hat{F}_{y,\text{VS}} &= L_y \int_{-\delta_\delta/2}^{\delta_\delta/2} dx \partial_x(\rho\nu\partial_x\Delta V_y) \\ &= \rho\nu(x=0) L_y \left[\partial_x \Delta V_y \right]_{-\delta_\delta/2}^{\delta_\delta/2}. \end{aligned} \quad (\text{B2})$$

In order to evaluate $\partial_x \Delta V_y$ at the boundaries of the dissipative layer, we need to solve for the ΔV_y profile of the bulk plasma in the time-asymptotic state. To do this, we solve

$$\begin{aligned} \nabla \cdot (\rho \nu \nabla \cdot \mathbf{V}) &= \partial_x (\rho \nu \partial_x V_y) = 0 \\ \Rightarrow \rho \nu \partial_x V_y &= \text{constant} \end{aligned} \quad (\text{B3})$$

in the two regions $-a < x < 0$ and $0 < x < a$, with boundary conditions $\Delta V_y(x=|a|) = 0$ consistent with no-slip boundaries and $\Delta V_y(x=0) = \Delta V_{y,\text{res}}$ characterizing the flow response at the resonant surface. In the region with $x > 0$, we solve Eq. (B3) by integrating from $0 \rightarrow a$ and $x \rightarrow a$ separately, then combine to obtain

$$\Delta V_y(0 < x < a) = \Delta V_{y,\text{res}} \frac{\sigma(x)}{\sigma(0)}, \quad (\text{B4})$$

where $\sigma(x)$ and $\sigma(0)$ correspond to integrals defined as

$$\sigma(x) = \int_x^a \frac{dx'}{\nu(x')}, \quad (\text{B5a})$$

$$\sigma(0) = \int_0^a \frac{dx'}{\nu(x')}. \quad (\text{B5b})$$

Similarly, integrations in the $x < 0$ range yield

$$\Delta V_y(-a < x < 0) = \Delta V_{y,\text{res}} \frac{\zeta(x)}{\zeta(0)}, \quad (\text{B6})$$

where $\zeta(x)$ and $\zeta(0)$ correspond to integrals defined as

$$\zeta(x) = \int_{-a}^x \frac{dx'}{\nu(x')}, \quad (\text{B7a})$$

$$\zeta(0) = \int_{-a}^0 \frac{dx'}{\nu(x')}. \quad (\text{B7b})$$

We then use Eqs. (B4) and (B6) to evaluate the limits in Eq. (B2). Upon taking the derivatives of the two integrals in the denominators, and recognizing that the integrals in the denominators are equal since $\nu(x)$ is an even function of x , we find the force per unit length of the \hat{y} component of the viscous force in the linear layer is

$$\hat{F}_{y,\text{VS}} = \frac{-2\rho\nu(x=0)L_y}{\nu_{\text{int}}a} \Delta V_{y,\text{res}}. \quad (\text{B8})$$

Here, ν_{int} is a dimensionless constant given by the integral

$$\nu_{\text{int}} = \frac{1}{a} \int_0^a \frac{dx'}{[1 + (\Delta_{\text{mag}}^{1/2} - 1)(x'/a)^{\Delta_{\text{width}}}]^2}. \quad (\text{B9})$$

This parameter captures the effect of the viscosity profile used in NIMROD computations, where $\nu_{\text{int}} = 0.431$ for the profile used in this work. Lastly, since we know that $L_y = 2\pi n/k_y$, this relation can be written as

$$\hat{F}_{y,\text{VS}} = -\frac{4\pi n\rho\nu(x=0)}{\nu_{\text{int}}ak_y} \Delta V_{y,\text{res}}. \quad (\text{B10})$$

-
- [1] A. Loarte, G. Saibene, R. Sartori, D. Campbell, M. Becoulet, L. Horton, T. Eich, A. Herrmann, G. Matthews, N. Asakura, et al., Plasma Phys. and Control. Fusion **45**, 1549 (2003).
- [2] T. C. Hender, J. C. Wesley, J. Bialek, A. Bondeson, A. H. Boozer, R. J. Buttery, A. Garofalo, T. P. Goodman, R. S. Granetz, Y. Gribov, et al., Nucl. Fusion **47**, S128 (2007).
- [3] T. E. Evans, R. A. Moyer, P. R. Thomas, J. G. Watkins, T. H. Osborne, J. A. Boedo, E. J. Doyle, M. E. Fenstermacher, K. H. Finken, R. J. Groebner, et al., Phys. Rev. Lett. **92**, 235003 (2004).
- [4] R. A. Moyer, T. E. Evans, T. H. Osborne, P. R. Thomas, M. Becoulet, J. Harris, K.-H. Finken, J. A. Boedo, E. J. Doyle, M. E. Fenstermacher, et al., Phys. Plasmas **12**, 056119 (2005).
- [5] T. E. Evans, R. A. Moyer, K. H. Burrell, M. E. Fenstermacher, I. Joseph, A. W. Leonard, T. H. Osborne, G. D. Porter, M. J. Schaffer, P. B. Snyder, et al., Nature Phys. **2**, 419 (2006).
- [6] T. Evans, M. Fenstermacher, R. Moyer, T. Osborne, J. Watkins, P. Gohil, I. Joseph, M. Schaffer, L. Baylor, M. Bécoulet, et al., Nucl. Fusion **48**, 024002 (2008).
- [7] R. M. Kulsrud and T. S. Hahm, Physica Scripta **T2B**, 525 (1982).
- [8] T. S. Hahm and R. M. Kulsrud, Phys. Fluids **28**, 2412 (1985).
- [9] H. P. Furth, J. Killeen, and M. N. Rosenbluth, Phys. Fluids **6**, 459 (1963).
- [10] P. H. Rutherford, Phys. Fluids **16**, 1903 (1973).
- [11] X. Wang and A. Bhattacharjee, Phys. Fluids B **4**, 1795 (1992).
- [12] F. W. Waelbroeck, Phys. Plasmas **1**, 2372 (1989).
- [13] G. E. Vekstein and R. Jain, Phys. Plasmas **5**, 1506 (1998).
- [14] R. Fitzpatrick and T. C. Hender, Phys. Fluids B **3**, 644 (1991).
- [15] R. Fitzpatrick, Nucl. Fusion **33**, 1049 (1993).
- [16] R. Fitzpatrick, Phys. Plasmas **5**, 3325 (1998).
- [17] F. L. Waelbroeck and R. Fitzpatrick, Phys. Rev. Lett. **78**, 1703 (1997).
- [18] R. Fitzpatrick and F. L. Waelbroeck, Phys. Plasmas **7**, 4983 (2000).
- [19] F. L. Waelbroeck, Phys. Plasmas **10**, 4040 (2003).
- [20] A. Cole and R. Fitzpatrick, Phys. Plasmas **13** (2006).
- [21] A. J. Cole, C. C. Hegna, and J. D. Callen, Phys. Rev. Lett. **99**, 065001 (2007).
- [22] A. J. Cole, C. C. Hegna, and J. D. Callen, Phys. Plasmas **15**, 056102 (2008).

- [23] R. Fitzpatrick and F. L. Waelbroeck, *Phys. Plasmas* **17**, 062503 (2010).
- [24] F. Waelbroeck, I. Joseph, E. Nardon, M. Bécoulet, and R. Fitzpatrick, *Nucl. Fusion* **52**, 074004 (2012).
- [25] W. Huang and P. Zhu, *Phys. Plasmas* **22**, 032502 (2015).
- [26] W. Huang and P. Zhu, *Phys. Plasmas* **23**, 032505 (2016).
- [27] C. Paz-Soldan, R. Nazikian, S. R. Haskey, N. C. Logan, E. J. Strait, N. M. Ferraro, J. M. Hanson, J. D. King, M. J. Lanctot, R. A. Moyer, et al., *Phys. Rev. Lett.* **114**, 105001 (2015).
- [28] R. Nazikian, C. Paz-Soldan, J. D. Callen, J. S. deGrassie, D. Eldon, T. E. Evans, N. M. Ferraro, B. A. Grierson, R. J. Groebner, S. R. Haskey, et al., *Phys. Rev. Lett.* **114**, 105002 (2015).
- [29] J. D. Callen, R. Nazikian, C. Paz-Soldan, N. M. Ferraro, M. T. Beidler, C. C. Hegna, and R. J. La Haye, report UW-CPTC 16-4, Dec. 20, 2016 (to be published).
- [30] M. W. Shafer, J. M. Canik, T. E. Evans, N. M. Ferraro, S. P. Hirshman, J. D. Lore, C. Chrystal, E. A. Unterberg, and A. Wingen, in *Bull. Am. Phys. Soc.* (Savannah, GA, 2015), vol. 60, p. Abstract TP12.00108.
- [31] F. Turco, Invited presentation, 43rd EPS Conference on Plasma Physics, Leuven, Belgium (July 2016).
- [32] J.-K. Park, A. H. Boozer, and A. H. Glasser, *Phys. Plasmas* **14**, 052110 (2007).
- [33] M. F. Heyn, I. B. Ivanov, S. V. Kasilov, W. Kernbichler, I. Joseph, R. A. Moyer, and A. M. Runov, *Nucl. Fusion* **48**, 024005 (2008).
- [34] Y. Liu, A. Kirk, and E. Nardon, *Phys. Plasmas* **17**, 122502 (2010).
- [35] N. M. Ferraro, *Phys. Plasmas* **19**, 056105 (2012).
- [36] Y. Q. Liu, A. Kirk, Y. Sun, P. Cahyna, I. T. Chapman, P. Denner, G. Fishpool, A. M. Garofalo, J. R. Harrison, E. Nardon, et al., *Plasma Phys. and Control. Fusion* **54**, 124013 (2012).
- [37] N. Ferraro, T. Evans, L. Lao, R. Moyer, R. Nazikian, D. Orlov, M. Shafer, E. Unterberg, M. Wade, and A. Wingen, *Nucl. Fusion* **53**, 073042 (2013).
- [38] S. R. Haskey, M. J. Lanctot, Y. Q. Liu, J. M. Hanson, B. D. Blackwell, and R. Nazikian, *Plasma Phys. and Control. Fusion* **56**, 035005 (2014).
- [39] S. R. Haskey, M. J. Lanctot, Y. Q. Liu, C. Paz-Soldan, J. D. King, B. D. Blackwell, and O. Schmitz, *Plasma Phys. and Control. Fusion* **57**, 025015 (2015).
- [40] Y. Liu, R. Akers, I. Chapman, Y. Gribov, G. Hao, G. Huijsmans, A. Kirk, A. Loarte, S. Pinches, M. Reinke, et al., *Nucl. Fusion* **55**, 063027 (2015).
- [41] J. Kim, S. S. Kim, and H. Jhang, *Phys. Plasmas* **23**, 092502 (2016).
- [42] T. Markovic, Y. Liu, P. Cahyna, R. Pánek, M. Peterka, M. Aftanas, P. Bílková, P. Bohm, M. Imříšek, P. Háček, et al., *Nucl. Fusion* **56**, 092010 (2016).
- [43] Y. Kikuchi, M. F. M. de Bock, K. H. Finken, M. Jakubowski, R. Jaspers, H. R. Koslowski, A. Kraemer-Flecken, M. Lehnen, Y. Liang, G. Matsunaga, et al. (TEXTOR-team), *Phys. Rev. Lett.* **97**, 085003 (2006).
- [44] Q. Yu, S. Günter, Y. Kikuchi, and K. Finken, *Nucl. Fusion* **48**, 024007 (2008).
- [45] V. Izzo and I. Joseph, *Nucl. Fusion* **48**, 115004 (2008).
- [46] H. Strauss, L. Sugiyama, G. Park, C. Chang, S. Ku, and I. Joseph, *Nucl. Fusion* **49**, 055025 (2009).
- [47] E. Nardon, P. Tamain, M. Bécoulet, G. Huysmans, and F. Waelbroeck, *Nucl. Fusion* **50**, 034002 (2010).
- [48] Q. Yu and S. Günter, *Nucl. Fusion* **51**, 073030 (2011).
- [49] F. Orain, M. Bécoulet, G. Dif-Pradalier, G. Huijsmans, S. Pamela, E. Nardon, C. Passeron, G. Latu, V. Grandgirard, A. Fil, et al., *Phys. Plasmas* **20**, 102510 (2013).
- [50] M. Bécoulet, F. Orain, G. T. A. Huijsmans, S. Pamela, P. Cahyna, M. Hoelzl, X. Garbet, E. Franck, E. Sonnendrücker, G. Dif-Pradalier, et al., *Phys. Rev. Lett.* **113**, 115001 (2014).
- [51] F. Orain, M. Bécoulet, J. Morales, G. T. A. Huijsmans, G. Dif-Pradalier, M. Hoelzl, X. Garbet, S. Pamela, E. Nardon, C. Passeron, et al., *Plasma Phys. and Control. Fusion* **57**, 014020 (2015).
- [52] F. Orain, M. Hölzl, E. Viezzer, M. Dunne, M. Bécoulet, P. Cahyna, G. Huijsmans, J. Morales, M. Willensdorfer, W. Suttrop, et al., *Nucl. Fusion* **57**, 022013 (2017).
- [53] N. Ivanov and A. Kakurin, *Nucl. Fusion* **57**, 016021 (2017).
- [54] N. V. Ivanov and A. M. Kakurin, *Phys. Plasmas* **21**, 102502 (2014).
- [55] W. Park, D. A. Monticello, and R. B. White, *Phys. Fluids* **27**, 137 (1984).
- [56] D. Biskamp, *Phys. Fluids* **29**, 1520 (1986).
- [57] O. A. Hurricane, T. H. Jensen, and A. B. Hassam, *Phys. Plasmas* **2**, 1976 (1995).
- [58] J. Rem and T. J. Schep, *Plasma Phys. and Control. Fusion* **40**, 139 (1998).
- [59] R. Fitzpatrick, *Phys. Plasmas* **10**, 2304 (2003).
- [60] A. Cole and R. Fitzpatrick, *Phys. Plasmas* **11**, 3525 (2004).
- [61] L. Comisso, D. Grasso, and F. L. Waelbroeck, *Phys. Plasmas* **22**, 042109 (2015).
- [62] K. Schindler and J. Birn, *J. Geophys. Res.* **98**, 15477 (1993).
- [63] P. K. Browning, J. Kawaguchi, K. Kusano, and G. E. Vekstein, *Phys. Plasmas* **8**, 132 (2001).
- [64] J. Birn, K. Galsgaard, M. Hesse, M. Hoshino, J. Huba, G. Lapenta, P. L. Pritchett, K. Schindler, L. Yin, J. Büchner, et al., *Geophys. Res. Lett.* **32** (2005).
- [65] C. Sovinec, A. Glasser, T. Gianakon, D. Barnes, R. Nebel, S. Kruger, D. Schnack, S. Plimpton, A. Tarditi, and M. Chu, *J. Comp. Phys.* **195**, 355 (2004).
- [66] C. Sovinec and J. King, *J. Comp. Phys.* **229**, 5803 (2010).
- [67] P. A. Sweet, in *Electromagnetic Phenomena in Cosmical Physics*, edited by B. Lehnert (Cambridge University Press, New York, 1958), p. 123.
- [68] E. N. Parker, *J. Geophys. Res.* **62**, 509 (1957).
- [69] R. Fitzpatrick, *Phys. Plasmas* **1**, 3308 (1994).
- [70] M. T. Beidler, C. C. Hegna, C. R. Sovinec, J. D. Callen, and N. M. Ferraro, in *Bull. Am. Phys. Soc.* (San Jose, CA, 2016), vol. 61, p. Abstract GP10.00076.
- [71] See <http://www.cptc.wisc.edu/Reports.html>.